Mathematical Modelling and Analysis
Volume 29, Issue 3, 575–599, 2024
https://doi.org/10.3846/mma.2024.20496

Solving a Spectral Problem for Large-Area Photonic Crystal Surface-Emitting Lasers

Mindaugas Radziunas[a], **Eduard Kuhn**[a] **and Hans Wenzel**[b]

[a] *Weierstrass Institute for Applied Analysis and Stochastics (WIAS)*
Mohrenstrasse 39, 10117 Berlin, Germany
[b] *Ferdinand-Braun-Institut (FBH)*
Gustav-Kirchhoff-Straße 4, 12489 Berlin, Germany
E-mail(*corresp.*): Mindaugas.Radziunas@wias-berlin.de
E-mail: Eduard.Kuhn@wias-berlin.de, Hans.Wenzel@fbh-berlin.de

Received November 29, 2023; accepted May 29, 2024

Abstract. We present algorithms for constructing and resolving spectral problems for novel photonic crystal surface-emitting lasers with large emission areas, given by first-order PDEs with two spatial dimensions. These algorithms include methods to overcome computer-arithmetic-related challenges when dealing with huge and small numbers. We show that the finite difference schemes constructed using relatively coarse numerical meshes enable accurate estimation of several major optical modes, which are essential in practical applications.

Keywords: modeling, finite difference, spectral problem, Green's function, exponential growth, simulations, semiconductor laser, photonic crystal.

AMS Subject Classification: 78M20; 78A60; 78-04; 35L02; 65N25; 65Y04.

1 Introduction

Semiconductor lasers (SLs) are small, efficient, relatively long-living, and cheap devices used in many modern applications, such as sensors requesting an enhanced coherence of light, optical communication systems demanding regular and stationary or irregular dynamics, or for material processing requiring up to a few kilowatt optical power. The emission of conventional high-power edge-emitting lasers [9, 13], however, has different beam divergence in vertical and lateral directions, so that the use of additional optical elements (lenses) for collimating the emitted fields is unavoidable. Despite that, even sophisticated

external optics can not improve the poor lateral beam quality induced by multiple lateral optical modes contributing to the emission of broad area lasers [12].

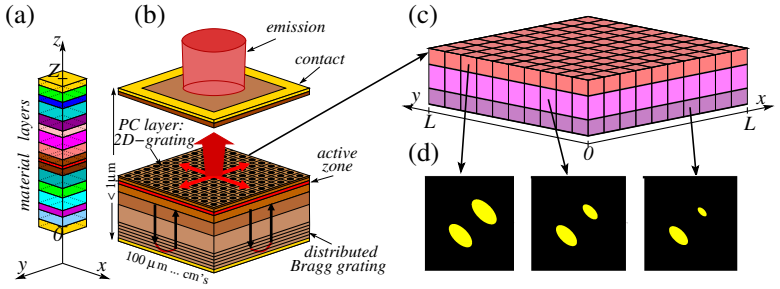

Figure 1. Schematics of photonic-crystal surface-emitting laser. (a): sandwiching of material layers along vertical ($z \in [0, Z]$) direction. (b): three-dimensional scheme. (c): lateral ($(x, y) \in [0, L] \times [0, L]$) PC layer consisting of three vertically-homogeneous sublayers. (d): structure of the elementary ($a \times a$)-large cell within each sublayer of the crystal.

In 1999, Prof. Susumu Noda and his group from Kyoto University proposed a Photonic-Crystal (PC) surface-emitting laser (SEL) [5], see Figure 1. The operation of this device is determined by the vertical structure of the SL (panels (a), (b)), the size and configuration of the PC layers (panel (c)), and the structure of unit cells of the PC (panel (d)). Whereas the vertical configuration should support a single *vertical* transverse-electric optical mode, the PC structure provides diffraction of the field in both lateral directions and its redirection towards the vertical output facet of the laser. Currently, the emission power of the best PCSELs [11] is comparable to that of the best edge emitters. In contrast to edge-emitting SLs, high-power PCSELs can have a single-mode-defined emission and possess radial symmetry and low emission divergence, which allows avoiding additional optical elements. Thus, modern PCSELs are comparable to or outperforming the best conventional edge-emitting SLs in many characteristics (besides the electrical-to-optical energy conversion efficiency) and have the potential to become preferable SLs in many applications.

A three-dimensional coupled wave theory [6, 7, 8, 11], a system of PDEs in temporal and two spatial directions, is used for modeling of PCSELs. However, matrix $\boldsymbol{C}$, which couples counter and cross-propagating optical fields within the PC, is not known explicitly; it should be constructed using parameters defined by integrals of yet-to-be-found functions. Even though the construction of $\boldsymbol{C}$ is well documented [6, 7], we could not find publications on fast and reliable algorithms for estimating the required integral parameters or discussing calculation efficiency when building $\boldsymbol{C}$. The estimation of these parameters is quite nontrivial. Due to small and large exponential terms $e^{\mp\mu z}$ entering the integral expressions, standard numerical integration techniques require fine discretizations, and, thus, are slow. Moreover, without the additional precautions to avoid too large exponential multipliers and too small terms in denominators, the parameter recovery fails when $|\mu|$ is too large. Thus, a detailed description of the efficient analytic-formula-based algorithms for calculating the composite parts of $\boldsymbol{C}$ working even when $|\mu| \gg 1$ is one of the main results of this work.

The best modern PCSELs rely on PCs composed of periodically made air holes within semiconductor layers. Due to the high refractive index contrast, already small PCSELs can emit light. However, field losses due to the combination of air and semiconductor material seem to be one of the reasons for the suboptimal efficiency of PCSELs. In contrast, large-size PCSELs not only allow achieving a higher emission power but also admit usage of all-semiconductor PC layers with less pronounced refractive index contrast (i.e., weaker coupling of optical field components by diffraction) and, possibly, smaller field losses and higher efficiency. Increasing the lateral size of PCSEL (factor L in Figure 1(c)) also requires adapting, developing, and analyzing numerical schemes used for solving model equations. In this work, we analyze the performance of the finite-difference schemes and spectral solvers applied to the field-equation-induced spectral problem. We show that a moderate refinement of the discretization mesh and the higher precision order schemes imply good precision of several dominant optical modes. This is the second important result of our paper.

Our work is structured as follows. In Section 2, we introduce a spectral problem for PCSELs. Subsection 2.1 presents a (1+2)-dimensional dynamic system of the first-order PDEs for slowly varying complex optical field amplitudes and a corresponding spectral problem used to define optical modes. Subsection 2.2 introduces a set of auxiliary problems and functions used for the construction of the effective parameters entering the model equations. Section 3 contains a collection of parameters, definitions, statements, and methods explored later to construct the field coupling matrix $\boldsymbol{C}$. The readers more interested in the problem's practical aspects can skip these preliminaries and directly proceed to the following Section 4, which presents algorithms for estimating of parameters used when constructing $\boldsymbol{C}$ and discusses the efficiency and precision of this construction in dependence on the complexity of the PCSEL's vertical configuration and the number of terms accounted for when truncating infinite series. Section 5 discusses numerical methods for solving the spectral problem. Here, we construct, apply, and analyze finite difference schemes of different precision. We show that the schemes constructed using coarse numerical meshes can provide acceptable precision for a few primarily important optical modes.

2 Mathematical model

2.1 Optical field equations and optical modes

The spatio-temporal dynamics in PCSELs is governed by the three-dimensional coupled-wave model [6, 7] derived from the Maxwell equations. The central part of this model, a system of PDEs for slowly varying field amplitudes $u(x,y,t) = (u^+, u^-)^T$, $v(x,y,t) = (v^+, v^-)^T$ (^{T}: the transpose), is given by

$$\begin{aligned} &\tfrac{1}{v_g}\tfrac{\partial}{\partial t}\begin{pmatrix} u \\ v \end{pmatrix} = \left[i\boldsymbol{C} - \begin{pmatrix} \boldsymbol{\sigma}\frac{\partial}{\partial x} & \boldsymbol{0} \\ \boldsymbol{0} & \boldsymbol{\sigma}\frac{\partial}{\partial y} \end{pmatrix} - i\Delta\beta \right] \begin{pmatrix} u \\ v \end{pmatrix}, \quad (x,y) \in [0,L]\times[0,L], \\ &\text{boundary conditions:} \quad u^+|_{x=0} = u^-|_{x=L} = v^+|_{y=0} = v^-|_{y=L} = 0. \end{aligned} \tag{2.1}$$

Here, L defines the lateral dimensions of the PCSEL, $v_g = c_0/n_g$ is the group velocity (c_0: speed of light in vacuum, n_g: group index), $\boldsymbol{\sigma} = \left(\begin{smallmatrix} 1 & 0 \\ 0 & -1 \end{smallmatrix}\right)$, $\boldsymbol{0}$ is a 2×2

zero matrix, whereas $\boldsymbol{C}$ is a nontrivial 4×4 field coupling matrix, which will be discussed in detail in the second part of this section. Finally, $\Delta\beta = \Delta\beta(N;T)$ is a carrier N- and temperature T-dependent relative propagation factor [13]. Its real part represents changes in the refractive index and, thus, deviation of the lasing frequency (or wavelength) from the reference frequency (wavelength λ_0). The imaginary part is defined by (N-dependent) optical amplification and losses within the PCSEL. The dependence of $\Delta\beta$ on self-heating in high-power SLs is essential. Due to significantly differing time scales of the photon, carrier, and temperature dynamics, T remains nearly unchanged within typically calculated time windows and should be accounted for parametrically [13]. On the contrary, temporal and spatial changes of N in dynamical simulations are crucial, such that one has to supplement the model with equations governing the carrier dynamics [6, 12]. If the current injected into a laser is switched on, N grows, causes changes of $\Delta\beta$, and, most importantly, implies growth of $\Im\Delta\beta$ until it reaches a threshold at which lasing begins. After this lasing threshold is reached, (averaged) N and $\Delta\beta$ remain approximately fixed, whereas further growth of electrical pumping induces growth of the emission's power. In the present paper, we are mainly interested in the study of the threshold behavior of PCSELs, where $\Delta\beta$ remains (nearly) uniform in space and stationary in time, thus can be well represented by a single complex constant $\overline{\Delta\beta}$.

For any fixed in time $\Delta\beta$, the field equations (2.1) define optical modes $(\Omega, \Phi(x,y))$. The four-component vector-eigenfunction $\Phi(x,y)$ provides spatial distributions of four field components. The real and imaginary parts of the complex frequency Ω represent the mode's relative frequency and damping, respectively. These modes can be found by substituting the ansatz

$$\begin{pmatrix} u(x,y,t) \\ v(x,y,t) \end{pmatrix} = \Phi(x,y)e^{i\Omega t}, \quad \Phi = \begin{pmatrix} \Phi_u \\ \Phi_v \end{pmatrix}, \quad \Phi_\nu = \begin{pmatrix} \Phi_\nu^+ \\ \Phi_\nu^- \end{pmatrix}, \quad \nu \in \{u, v\} \tag{2.2}$$

into Equations (2.1) and resolving the resulting spectral problem

$$\begin{aligned} &\Big[i\boldsymbol{C} - \begin{pmatrix} \boldsymbol{\sigma}\frac{\partial}{\partial x} & \boldsymbol{0} \\ \boldsymbol{0} & \boldsymbol{\sigma}\frac{\partial}{\partial y} \end{pmatrix} - \Lambda\Big]\Phi = 0, \qquad (x,y) \in [0,L]\times[0,L], \\ &\Lambda = i(\overline{\Delta\beta} + \tfrac{\Omega}{v_g}), \quad \Phi_u^+(0,y) = \Phi_u^-(L,y) = \Phi_v^+(x,0) = \Phi_v^-(x,L) = 0. \end{aligned} \tag{2.3}$$

Here, we exploit our assumption of spatially uniform distribution of $\Delta\beta = \overline{\Delta\beta}$, which allows combining the complex optical frequency Ω and the complex factor $\overline{\Delta\beta}$ into a single complex eigenvalue Λ. $-\Re\Lambda$ represents the threshold of the mode, i.e., the value of $\Im\overline{\Delta\beta}$ at which the mode damping $\Im\Omega$ vanishes.

The spectral problem (2.3) defines multiple optical modes (Λ, Φ) and is vital when designing PCSEL devices. Mode with the largest but still negative $\Re\Lambda$ (the main mode) is excited first when up-tuning the bias current, which causes an increase of $\Im\overline{\Delta\beta}$. The damping $\Im\Omega$ of this mode vanishes; a threshold of this mode is the lasing threshold, $-\Re\Lambda_1 = [\Im\Delta\beta]_{\rm th}$; the remaining modes have positive $\Im\Omega$, i.e., $\Re\Lambda_{\rm rest} < \Re\Lambda_1$, and remain damped. In practical applications, PCSELs should have a small lasing threshold (large $\Re\Lambda_1$), and a large threshold gap to other modes (large $\Re(\Lambda_1 - \Lambda_{\rm rest})$, which is needed for a desired single-mode lasing. Besides, when analyzing separate modes, one can be interested

in the balance of the generated intensity, losses within and at the lateral edges of the PCSEL, and radiation in the vertical to PC and QW layers direction. Equation (2.3) allows relating integral factors $\mathcal{I}_l$ (losses at the lateral borders), $\mathcal{I}_g$, and $\mathcal{I}_v$ (mainly determined by the generated and vertically radiated field intensity but also include field losses inside the PCSEL) [7].

Lemma 1. *Let Λ and the nontrivial four-component vector-function $\Phi(x,y)$ satisfy Equation* (2.3)*. Then the following integral balance relations hold:*

$$\begin{aligned} &\mathcal{I}_g = \mathcal{I}_v + \mathcal{I}_l, \qquad \text{where} \qquad \mathcal{I}_g = -2\Re\Lambda \left\|\Phi\right\|^2, \quad \mathcal{I}_v = 2\Im(\Phi, \boldsymbol{C}\Phi), \\ &\mathcal{I}_l = \int_0^L |\Phi_u^+(L,y)|^2 + |\Phi_u^-(0,y)|^2 dy + \int_0^L |\Phi_v^+(x,L)|^2 + |\Phi_v^-(x,0)|^2 dx. \end{aligned} \tag{2.4}$$

Here $(\xi,\zeta) = \int_0^L\int_0^L \sum_{j=1}^{\dim\{\xi,\zeta\}} \xi_j^*(x,y)\zeta_j(x,y)dxdy$ is the scalar product of vector-functions ξ and ζ, and $\|\xi\| = (\xi,\xi)^{1/2}$ is a corresponding norm of ξ.

Proof. The relations (2.4) can be obtained after scalar multiplication of both sides of Equation (2.3) by 2Φ and taking the real part of the resulting equation. □

2.2 Coupling of the optical fields

The matrix $\boldsymbol{C}$ depends on the laser's vertical structure, see Figure 1(a)-(c), the PC unit cells' size (latice constant a) and shape, Figure 1(d), and the real squared refractive index $\bar{n}^2(x,y,z)$, which is a part of the complex dielectric constant $\bar{\epsilon}(x,y,z) = \bar{n}^2(x,y,z) + \Delta\epsilon(x,y,z)$ in each material layer, Figure 1(a). Here, complex $\Delta\epsilon$ includes the material's absorption and carrier- and temperature-induced corrections of $\bar{\epsilon}$. Lasing of PCSELs can be achieved only when $\lambda_0 \approx a\, n_\bullet$ ($n_\bullet$: effective refractive index of the main vertical optical mode).

The PCSEL device is sandwiched from m vertically homogeneous material layers $\bar{S}_k$ along the vertical coordinate z, see Figure 1(a). Let

$$\begin{aligned} &S_k = (z_{k-1}, z_k), \quad \bar{S}_k = [z_{k-1}, z_k], \quad \cup_{k=1}^m \bar{S}_k = [0, Z], \\ &|S_k| = z_k - z_{k-1}, \quad \bar{z}_k = \tfrac{z_{k-1}+z_k}{2}, \ k = 1, \dots, m, \\ &S_{\mathrm{L}} \equiv S_0 = (-\infty, 0), \qquad S_{\mathrm{U}} \equiv S_{m+1} = (Z, +\infty), \end{aligned}$$

where $z_0 = 0$, $z_m = Z$, and other z_k are interfaces of corresponding layers. Here and in the following, the indices L and U indicate that the functions or parameters are assigned to the lower or upper part of the infinitely extended vertical domain or individual material layers. Each layer is either laterally homogeneous with a real refractive index $n_k \equiv \bar{n}(x,y,z)|_{z\in S_k}$ or a PC with a pair of real indices (n_k^I, n_k^{II}) representing the material within the PC feature (e.g., air with $n_k^{II} \approx 1$ [6, 7]) and surrounding semiconductor material, respectively. Within the PC, n_k^2 is the spatial average of $\bar{n}^2$ over the unit cell:

$$n_k^2 = \frac{1}{a^2}\int_{-a/2}^{a/2}\int_{-a/2}^{a/2} \bar{n}^2(x,y,z)|_{z\in S_k} dxdy.$$

The real positive piece-wise function $n(z)$, $n(z)|_{z\in S_k} = n_k$, $k = 1, \dots, m$, represents the (laterally-averaged) refractive index of each material layer, including PC layers. Real refractive indices of the infinitely broad lower (S_{L}) and upper (S_{U}) materials surrounding the PCSEL device are denoted as n_{L} and n_{U}. Here we assume that the outer material is air, i.e., $n_{\mathrm{L}} = n_{\mathrm{U}} \approx 1$. n_{L}, n_{U} and the function $n(z)$ define the layer-wise constant function $\sigma(z)$ and factors σ_{L}, σ_{U},

$$\begin{array}{l} \sigma(z)|_{z\in S_j} = \sigma_j \stackrel{def}{=} \tilde{\sigma}(n_\bullet, n_j), \quad j = \{1, \dots, m\} \cup \{\mathrm{L}, \mathrm{U}\}, \\ \text{where} \qquad \tilde{\sigma}(\xi, \zeta) = k_0 \sqrt{\xi^2 - \zeta^2} \in \mathbb{C}, \quad \Re\tilde{\sigma}(\xi, \zeta) \geq 0, \quad k_0 \stackrel{def}{=} \frac{2\pi}{\lambda_0}, \end{array} \tag{2.5}$$

exploited in the one-dimensional Helmholtz problem

$$\tfrac{d^2}{dz^2}\Theta(z) - \sigma^2(z)\Theta(z) = 0, \qquad z \in [0, Z], \quad \sigma^2(z) \in \mathbb{R}, \tag{2.6}$$

satisfying homogeneous Dirichlet ($\rho = 0$) or natural radiating ($\rho = 1$) boundary conditions (BCs) at $z = 0$ and $z = Z$:

$$\rho\tfrac{d\Theta}{dz}(0) = \sigma_{\mathrm{L}}\Theta(0), \ \rho\tfrac{d\Theta}{dz}(Z) = -\sigma_{\mathrm{U}}\Theta(Z), \quad \sigma_{\mathrm{L}}, \sigma_{\mathrm{U}} \in \mathbb{R}_+ \cup 0. \tag{2.7}$$

Within each S_k, function $\Theta(z)$ can be written as a linear combination of two special solutions $\theta_k^+(z)$ and $\theta_k^-(z)$ to a linear homogeneous Equation (2.6):

$$\begin{array}{l} \Theta(z)|_{z\in S_k} = (\mathcal{B}_k^\Theta)^T \theta_k(z), \quad \mathcal{B}_k^\Theta \stackrel{def}{=} \begin{pmatrix} \Theta(z_k) \\ \Theta(z_{k-1}) \end{pmatrix}, \quad \theta_k = \begin{pmatrix} \theta_k^+ \\ \theta_k^- \end{pmatrix}, \\ \theta_k^\pm|_{z\in S_k} \text{ satisfy Equation (2.6)}, \quad \theta_k(z_k) = \binom{1}{0}, \quad \theta_k(z_{k-1}) = \binom{0}{1}. \end{array} \tag{2.8}$$

Equations (2.6), (2.7) with σ from Equation (2.5) define the real effective refractive index $n_\bullet \in (0, \max_z n(z)]$ and the corresponding vertical mode $\Theta(z)$, normalized by $\int_{\mathbb{R}} |\Theta(z)|^2 dz = 1$. In typical applications, $n_\bullet$ is between 3 and 4, such that BCs (2.7) for $\rho = 1$ and $n_{\mathrm{L}} = n_{\mathrm{U}} \approx 1$ represent at $z \to \pm\infty$ vanishing optical fields. Non-vanishing Fourier expansion coefficients within the PC layers S_j,

$$\xi_{r,s}^j = \frac{1}{a^2} \int_{-a/2}^{a/2} \int_{-a/2}^{a/2} \bar{n}^2(x, y, z)|_{z\in S_j} e^{i2\pi(rx+sy)/a} dxdy, \quad r, s \in \mathbb{Z} \setminus 0, \tag{2.9}$$

together with the PC-layer-wise integrals and related 2×2 matrices $\boldsymbol{p}_j$, $\boldsymbol{g}_{(r,s)}^{(k,j)}$,

$$\begin{array}{l} \mathcal{P}_j^\Theta = \int_{S_j} |\Theta(z)|^2 dz = (\mathcal{B}_j^\Theta)^T \boldsymbol{p}_j \mathcal{B}_j^{\Theta^*}, \quad \boldsymbol{p}_j \stackrel{def}{=} \int_{S_j} \theta_j(z) \theta_j^{*T}(z) dz, \\ \mathcal{G}_{(r,s)}^{(k,j)} = \int_{S_k} \int_{S_j} G_{(r,s)}(z, z') \Theta(z') dz' \, \Theta^*(z) dz = (\mathcal{B}_j^\Theta)^T \boldsymbol{g}_{k,j} \mathcal{B}_k^{\Theta^*}, \\ \boldsymbol{g}_{(r,s)}^{(k,j)} \stackrel{def}{=} \int_{S_k} \int_{S_j} \theta_j(z') G_{(r,s)}(z, z') dz' \, \theta_k^{*T}(z) dz, \quad r, s \in \mathbb{Z}, \end{array} \tag{2.10}$$

are used to construct the coupling matrix $\boldsymbol{C}$. Green's functions $G_p(z, z')$ with $p \stackrel{def}{=} (r, s)$ and $|p|^2 \stackrel{def}{=} r^2 + s^2$ solve the inhomogeneous problem [8]

$$\tfrac{\partial^2}{\partial z^2} G_p(z, z') - \sigma_p^2(z) G_p(z, z') = -\delta(z - z'), \ (z, z') \in [0, Z] \times [0, Z], \tag{2.11}$$

with radiating boundary conditions

$$\frac{\partial G_p(0,z')}{\partial z} = \sigma_{p,L} G_p(0,z'), \qquad \frac{\partial G_p(Z,z')}{\partial z} = -\sigma_{p,U} G_p(Z,z'). \tag{2.12}$$

$\delta(\zeta)$ in Equation (2.11) is the Dirac's delta-function, whereas σ_p is defined by

$$\sigma_p(z) = \tilde{\sigma}(\tfrac{|p|\lambda_0}{a}, n(z)),\ \sigma_{p,j} = \tilde{\sigma}(\tfrac{|p|\lambda_0}{a}, n_j),\ j \in \{1,\dots,m\} \cup \{\mathrm{L},\mathrm{U}\}.$$

Since $\frac{\lambda_0}{a} \approx n_\bullet$, for $|p| = 1$ (not used when building $\boldsymbol{C}$), the left-hand side of Equation (2.11) reminds that of Equation (2.6). At $z = z' \pm 0$, Equation (2.11) implies

$$G_p(z'+0,z') = G_p(z'-0,z'), \quad \frac{\partial G_p(z'+0,z')}{\partial z} = \frac{\partial G_p(z'-0,z')}{\partial z} - 1. \tag{2.13}$$

In typical applications, for $|p| > 1$, $\sigma_{p,j}$ are strictly positive real, such that BCs (2.12) imply the convergence of $|G_p(z,z')|$ to zero when $z \to \pm\infty$. When $|p| = 0$, the real parts of $\sigma_{p,L}$ and $\sigma_{p,U}$ are absent, such that the radiated fields preserve their intensity outside the domain $[0,Z]$. In this case, we use $\sigma_{p,j} = ik_0|n_j|$, $j \in \{\mathrm{L},\mathrm{U}\}$, which reminds us of Sommerfeld's radiation conditions, even though those are formulated only for two- and three-dimensional cases.

Matrix $\boldsymbol{C}$ is defined as an infinite sum of simpler 4×4-dimensional matrices, which are functions of $\mathcal{G}_{(r,s)}$, $\mathcal{P}^{\Theta}$, and $\xi_{r,s}$:

$$\begin{aligned} &\boldsymbol{C} = \boldsymbol{C}_{1D}(\mathcal{P}^{\Theta}, \xi_{\pm2,0}, \xi_{0,\pm2}) + \boldsymbol{C}_{\mathrm{rd}}(\mathcal{G}_{(0,0)}, \xi_{\pm1,0}, \xi_{0,\pm1}) + \boldsymbol{C}_{2D}, \\ &\boldsymbol{C}_{2D} = \textstyle\sum_{|r|+|s|>1} \boldsymbol{C}_{2D}^{(r,s)}(\mathcal{G}_{(r,s)}, \mathcal{P}^{\Theta}, \xi_{r\pm1,s}, \xi_{r,s\pm1}). \end{aligned} \tag{2.14}$$

$\boldsymbol{C}_{\mathrm{rd}}$ is responsible for the outcoupling of the radiated light. For considered real-valued $\bar{n}^2$, $\boldsymbol{C}_{1D}$ is a Hermitian matrix, inducing coupling of counter propagating fields only, whereas another Hermitian matrix $\boldsymbol{C}_{2D}$ incorporates all higher-order effects, including cross-coupling of fields, which is necessary for achieving high quality of radiation. For more details on the definition of $\boldsymbol{C}$, see [6,7].

Remark 1. Since $\boldsymbol{C}_{1D}$ and $\boldsymbol{C}_{2D}$ in Equation (2.14) are Hermitian, i.e., $\boldsymbol{C} - \boldsymbol{C}^{*T} = \boldsymbol{C}_{\mathrm{rd}} - \boldsymbol{C}_{\mathrm{rd}}^{*T}$, the integral factor $\mathcal{I}_v$ in Equation (2.4) can be reformulated as

$$\mathcal{I}_v = 2\Im\big(\Phi, \boldsymbol{C}\Phi\big) = -\big(\Phi, i[\boldsymbol{C} - \boldsymbol{C}^{*T}]\Phi\big) = 2\Im\big(\Phi, \boldsymbol{C}_{\mathrm{rd}}\Phi\big),$$

i.e., is determined only by the radiative component of the matrix $\boldsymbol{C}$.

3 Preliminaries

In this section, we introduce a set of new parameters and statements, which are actively explored when constructing the field coupling matrix $\boldsymbol{C}$.

3.1 Large and small number problem

The main numerical cost in estimating $\boldsymbol{C}$ is calculations of the double integrals $\mathcal{G}_{(r,s)}^{(k,l)}$ in Equation (2.10) for large sets of parameters (r,s). Estimation of these integrals using numerically discretized functions $\Theta(z)$ and $G_{(r,s)}(z,z')$ is

inefficient, especially when $|p|$ is large, which causes a very fast exponential growth and decay of $|G_{(r,s)}(z,z')|$ at $z \approx z'$. Luckily, provided $n_\bullet$ is known, θ and $G_{(r,s)}$ can be written as linear combinations of exponentials[1]

$$\begin{cases} e^{\sigma_j(z-\bar{z}_j)}, \quad e^{-\sigma_j(z-\bar{z}_j)} & \text{for } \theta_j(z) \text{ in } S_j, \\ e^{\nu\sigma_{p,k}(z-\bar{z}_j)} e^{\nu'\sigma_{p,j}(z'-\bar{z}_j)}, \ \nu,\nu' \in \pm & \text{for } G_p^{(k,j)}(z,z') \text{ in } S_k \times S_j, \end{cases} \tag{3.1}$$

and the matrices $\boldsymbol{p}_j$, $\boldsymbol{g}_p^{(k,j)}$ in Equation (2.10) admit analytic expressions relying on their integrals. Still, these expressions rely on possibly huge and almost vanishing exponentials $e^{\sigma_{\cdot,j}|S_j|}$ and corresponding sinh and cosh functions, which can not be properly handled by computer arithmetics. To avoid numerical problems even when $\sigma_j \to 0$ (not a very probable case in realistic problems, achievable only when $n_\bullet = n_j$) or $e^{\sigma_{\cdot,j}|S_j|} \to \infty$ (unavoidable in calculations of Green's function with large $|p|$ and large positive σ), we introduce new notations:

$$\begin{aligned} &(1-\Gamma_j) \overset{def}{=} \tfrac{2e^{-\sigma_j|S_j|}}{1+e^{-\sigma_j|S_j|}}, \qquad \Gamma_j = 1-(1-\Gamma_j) = \tanh\tfrac{\sigma_j|S_j|}{2}, \\ &\text{such that} \quad \Re\Gamma_j \geq 0, \quad \Gamma_j \overset{\sigma_j\to 0}{\longrightarrow} 0, \quad \tfrac{\Gamma_j}{\sigma_j} \overset{\sigma_j\to 0}{\longrightarrow} \tfrac{|S_j|}{2}, \quad \Gamma_j \overset{\Re\sigma_j|S_j|\gg 1}{\longrightarrow} 1. \end{aligned} \tag{3.2}$$

In practical calculations, we define first $1-\Gamma_j$ (almost zero when $\Gamma_j \approx 1$) and only then Γ_j and the remaining Γ_j-dependent expressions. In this way, we can keep a tiny but still non-vanishing factor $1-\Gamma_j$, which could otherwise be lost due to computer arithmetics[2]. When formulating our algorithms, we eliminate this possibly tiny term from the denominators of all formulas.

3.2 Transfer matrices

When building $\boldsymbol{C}$, we solve Equations (2.6) and (2.11), both related to the equation

$$F''(z) - \sigma^2(z)F(z) = 0, \qquad z \in \cup_{j=1}^m S_j, \tag{3.3}$$

where $\sigma(z)$ is a complex layer-wise constant function,

$$\sigma(z)_{z\in S_j} = \sigma_j \in \mathbb{C}, \quad \sigma_j^2 \in \mathbb{R}, \quad \Re\sigma_j \geq 0, \quad j \in \{1,\ldots,m\}. \tag{3.4}$$

Below, we give several formulas for translating F and F' between spatial positions z and z' by transfer matrices [2] and present algorithms for avoiding possibly huge exponentials $|e^{\sigma_j|S_j|}|$ in calculations. These formulas and algorithms are used for constructing the vertical mode function $\Theta(z)$, Green's functions $G_p(z,z')$, and required integral expressions of these functions.

[1] In general, it is possible that $n_\bullet = n_k$ in specific layers S_k, such that $\sigma_k = 0$, and instead of exponentials (3.1), we have to use linear w.r.t. z functions. In most cases, the formulas derived below for nonzero σ_k can be corrected by taking their limit with $\sigma_k \to 0$. Factors $\sigma_{p,k}$ used to construct Green's functions are never zero in real applications.

[2] For example, $e^{-2\sigma_j|S_j|}$ can be of order 10^{-100} and still be treated correctly in multiplicative expressions in the computer code. However, nominally the same number $(e^{-2\sigma_j|S_j|}+1)-1$ can be treated as zero during the calculations.

Lemma 2. *Assume that $F(z) \in C^2(S_j)$ satisfies Equations* (3.3), (3.4), *and $\mathcal{B}_j^F$ (i.e., $F(z_{j-1})$ and $F(z_j)$) are known. Then, according to Equation* (2.8),

$$F(z) = (\mathcal{B}_j^F)^T \theta_j(z), \text{ where } \theta_j = \begin{pmatrix} \theta_j^+ \\ \theta_j^- \end{pmatrix}, \ \theta_j^{\pm}(z) = \frac{\pm \sinh \sigma_j (z - \bar{z}_j \pm |S_j|/2)}{\sinh \sigma_j |S_j|}. \quad (3.5)$$

If instead of $F(z_j)$ (or $F(z_{j-1})$) we have $F'(z_{j-1})$ (or $F'(z_j)$), the vector $\binom{F}{F'}(z)$ at any $z \in S_j$ can be written using transfer matrices:

$$\begin{gathered} \begin{pmatrix} F \\ F' \end{pmatrix}(z) = \boldsymbol{M}_j(z, z_{j-1}; \sigma_j) \begin{pmatrix} F \\ F' \end{pmatrix}(z_{j-1}) = \boldsymbol{M}_j(z, z_j; \sigma_j) \begin{pmatrix} F \\ F' \end{pmatrix}(z_j), \\ \boldsymbol{M}_j(z, \tilde{z}; \sigma_j)|_{z,\tilde{z} \in \bar{S}_j} \stackrel{def}{=} \begin{pmatrix} \cosh(\sigma_j(z - \tilde{z})) & \sinh(\sigma_j(z - \tilde{z}))/\sigma_j \\ \sigma_j \sinh(\sigma_j(z - \tilde{z})) & \cosh(\sigma_j(z - \tilde{z})) \end{pmatrix}. \end{gathered} \quad (3.6)$$

When $\sigma_j \to 0$, expressions $\frac{\sinh \sigma_j \xi}{\sinh \sigma_j |S_j|}$ within $\theta_j(z)$ in Equation (3.5) *should be replaced by $\frac{\xi}{|S_j|}$, and $\boldsymbol{M}_j(z, \tilde{z}; \sigma_j)$ in* (3.6) *by the matrix $\left(\begin{smallmatrix} 1 & z - \tilde{z} \\ 0 & 1 \end{smallmatrix}\right)$.*

Proof. One can easily check that the expressions for $\theta_j(z)$ in (3.5) and $F(z)$ in (3.6) satisfy Equation (3.3), whereas at the edges of S_j, $\theta_j(z)$ fulfills Equation (2.8). Since the second-row elements of $\boldsymbol{M}_j$ in (3.6) are z-derivatives of the corresponding first-row elements, $\boldsymbol{M}_j$ provides a correct expression of $F'(z)$ along S_j. The expressions for $\sigma_j \to 0$ follow directly from the relation $\lim_{\xi \to 0} \frac{\sinh \xi}{\xi} = 1$. □

Remark 2. Transfer matrices are invertible, $\boldsymbol{M}_j(z, \tilde{z}; \sigma_j) = \boldsymbol{M}_j^{-1}(\tilde{z}, z; \sigma_j)$, and can be combined with each other, $\boldsymbol{M}_j(z, \tilde{z}; \sigma_j) = \boldsymbol{M}_j(z, z'; \sigma_j) \boldsymbol{M}_j(z', \tilde{z}; \sigma_j)$. In both these cases we assume that $z, z', \tilde{z} \in \bar{S}_j$.

Corollary 1. A complex conjugate of $F(z)$ satisfying all conditions of Lemma 2 is given by Equation (3.5) using $\mathcal{B}_j^{F^*}$ instead of $\mathcal{B}_j^F$.

Proof. We can easily show that the vector-function $\theta_j(z)$ in Equation (3.5) is real, which immediately proves our statement. Recall that $\sigma_j^2 \in \mathbb{R}$. For $\sigma_j^2 > 0$, we have $\sigma_j > 0$ and $\frac{\sinh \sigma_j \xi}{\sinh \sigma_j |S_j|} \in \mathbb{R}$. When $\sigma_j^2 < 0$, $\sigma_j = i|\sigma_j|$ and the same expressions can be written as $\frac{\sin |\sigma_j| \xi}{\sin |\sigma_j| |S_j|} \in \mathbb{R}$. □

Corollary 2. Matrix $\boldsymbol{p}_j$ introduced in Equation (2.10) can be written as

$$\boldsymbol{p}_j \stackrel{def}{=} \begin{pmatrix} p_j^+ & p_j^- \\ p_j^- & p_j^+ \end{pmatrix}, \ p_j^{\pm} = \frac{2[\Gamma_j^2 \pm 1] + [\Gamma_j^2 \mp 1](1 - \Gamma_j^2)|S_j| \frac{\sigma_j}{\Gamma_j}}{8 \sigma_j \Gamma_j} \stackrel{\sigma_j \to 0}{\to} \frac{(3 \pm 1)|S_j|}{12}. \quad (3.7)$$

Proof. According to Corollary 1, θ_j defined in Equation (3.5) is real, i.e., $\theta_j = \theta_j^*$. Integration of $\theta_j^+ \theta_j^-$, $(\theta_j^+)^2$, and $(\theta_j^-)^2$ over S_j imply expressions (3.7). The limit of these expressions for $\sigma_j \to 0$ can be found using L'Hopital's rule. □

3.3 Translation of boundary conditions

Lemma 3. *Assume that the complex function* $F(z) \in C^2(\cup_{j=1}^m S_j) \cup C^1([0,Z])$ *satisfies the problem* (3.3), (3.4). *Then, we can construct composite transfer matrices* $\boldsymbol{M}(z_l, z_k; \sigma)$, *translating the vector* $\binom{F}{F'}(z)$ *between any layer interfaces* z_k *and* z_l, $0 \le k, l \le m$. *If* $\{S_j\}$ *are all layers between* z_k *and* z_l, *the composite matrix elements can be written as linear combinations of all different products of exponentials* $e^{\pm\sigma_j |S_j|}$.

Proof. For simplicity, let us assume that $z_l > z_k$, such that $\{S_j\}$ are all layers with indices $j = k+1, \dots, l$. Because of the continuity of F and F', transfer matrices (3.6) can also be used at the layer borders, which also are borders of the neighboring layer S_{j-1} or S_{j+1}. By superposing layer-wise transfer matrices $\boldsymbol{M}_j$, we construct the required overall transfer matrix,

$$\boldsymbol{M}(z_l, z_k; \sigma) = \boldsymbol{M}_l(z_l, z_{l-1}; \sigma_l) \cdots \boldsymbol{M}_{k+1}(z_{k+1}, z_k; \sigma_{k+1}), \tag{3.8}$$

propagating $\binom{F}{F'}(z)$ from z_k to z_l. Each of submatrices $\boldsymbol{M}_j$ is determined by combinations of $e^{-\sigma_j |S_j|}$ and $e^{+\sigma_j |S_j|}$ (or just constants 0, 1, $|S_j|$ if $\sigma_j \to 0$). Thus, the elements of the overall matrix are as suggested in this lemma. An invertibility of each $\boldsymbol{M}_j$, see Remark 2, allows us to construct an inverse matrix $\boldsymbol{M}^{-1}(z_l, z_k; \sigma) = \boldsymbol{M}(z_k, z_l; \sigma) = \boldsymbol{M}_{k+1}(z_k, z_{k+1}; \sigma_{k+1}) \cdots \boldsymbol{M}_l(z_{l-1}, z_l; \sigma_l)$. □

Corollary 3. We can rewrite matrices $\boldsymbol{M}(z_l, z_k; \sigma)$ with $k \neq l$ in Equation (3.8) as

$$\begin{aligned}
&\boldsymbol{M}(z_l, z_k; \sigma) = \left[\prod_{j=\min\{l,k\}+1}^{\max\{l,k\}} e^{\sigma_j |S_j|}\right] \boldsymbol{M}_{[l,k]}^{\dagger\,\mathrm{sgn}(l-k)}(\sigma), \\
&\boldsymbol{M}_{[l,k]}^{\dagger\nu}(\sigma) = \begin{cases} \boldsymbol{M}_{[l]}^{\dagger\nu}(\sigma_l) \cdots \boldsymbol{M}_{[k+1]}^{\dagger\nu}(\sigma_{k+1}) & \text{for } \nu = + \\ \boldsymbol{M}_{[l+1]}^{\dagger\nu}(\sigma_{l+1}) \cdots \boldsymbol{M}_{[k]}^{\dagger\nu}(\sigma_k) & \text{for } \nu = - \end{cases}, \quad \text{where} \\
&\boldsymbol{M}_{[j]}^{\dagger\pm}(\sigma_j) \overset{def}{=} \tfrac{1}{(1+\Gamma_j)^2} \begin{pmatrix} 1+\Gamma_j^2 & \pm 2\Gamma_j/\sigma_j \\ \pm 2\sigma_j \Gamma_j & 1+\Gamma_j^2 \end{pmatrix} \overset{\sigma_j \to 0}{\longrightarrow} \begin{pmatrix} 1 & \pm|S_j| \\ 0 & 1 \end{pmatrix},
\end{aligned} \tag{3.9}$$

such that the reduced matrices $\boldsymbol{M}^\dagger$ do not depend on possibly huge $|e^{\sigma_j |S_j|}|$.

Proof. The statement follows directly from Equations (3.8), (3.6), and (3.2). □

Lemma 4. *Matrices* $\boldsymbol{M}^\dagger$ *translate Robin BCs*

$$F'(0) = \sigma_{\mathrm{L}} F(0), \qquad F'(Z) = -\sigma_{\mathrm{U}} F(Z), \tag{3.10}$$

of Equations (3.3) *and* (3.4) *to similar conditions at any material layer interface* z_j, $j = 1, \dots, m-1$*:*

$$\begin{aligned}
F'(z_j) &= \eta_{j+1}^{\mathrm{L}} F(z_j), \qquad \eta_{j+1}^{\mathrm{L}} = \tfrac{M_{[j,0],21}^{\dagger+}(\sigma) + \sigma_{\mathrm{L}} M_{[j,0],22}^{\dagger+}(\sigma)}{\sigma_{\mathrm{L}} M_{[j,0],12}^{\dagger+}(\sigma) + M_{[j,0],11}^{\dagger+}(\sigma)}, \\
F'(z_j) &= -\eta_j^{\mathrm{U}} F(z_j), \qquad \eta_j^{\mathrm{U}} = \tfrac{M_{[j,m],21}^{\dagger-}(\sigma) - \sigma_{\mathrm{U}} M_{[j,m],22}^{\dagger-}(\sigma)}{\sigma_{\mathrm{U}} M_{[j,m],12}^{\dagger-}(\sigma) - M_{[j,m],11}^{\dagger-}(\sigma)}.
\end{aligned} \tag{3.11}$$

Proof. Equations (3.11) can be easily derived by relating the vectors $\binom{F}{F'}(0)$ or $\binom{F}{F'}(Z)$ with $\binom{F}{F'}(z_j)$ using transfer matrices $\boldsymbol{M}(z_j, z_0; \sigma)$ or $\boldsymbol{M}(z_j, z_m; \sigma)$, see Equation (3.8), exploring the reduced form of $\boldsymbol{M}$ given in Equation (3.9), and solving the resulting equations together with the BCs (3.10). □

Remark 3. To avoid problems induced by computer arithmetics when working with almost vanishing numbers, for calculations of factors η^{L} and η^{U}, one should better use the recurrent expressions, which do not fail even when in some S_j $\Gamma_j \to 1$ and still are well defined when $|\sigma_j| \to 0$ and $\Gamma_j \to 0$:

$$\begin{aligned} &\eta_1^{\mathrm{L}} = \sigma_{\mathrm{L}}, \quad \left[\eta_{j+1}^{\mathrm{L}} - \sigma_j\right] = \frac{(\eta_j^{\mathrm{L}} - \sigma_j)(1-\Gamma_j)^2}{(1+\Gamma_j^2)+\frac{2\Gamma_j}{\sigma_j}\eta_j^{\mathrm{L}}} \overset{\sigma_j \to 0}{\longrightarrow} \frac{\eta_j^{\mathrm{L}}}{1+|S_j|\eta_j^{\mathrm{L}}}, \ 1 \le j < m, \\ &\eta_m^{\mathrm{U}} = \sigma_{\mathrm{U}}, \quad \left[\eta_{j-1}^{\mathrm{U}} - \sigma_j\right] = \frac{(\eta_j^{\mathrm{U}} - \sigma_j)(1-\Gamma_j)^2}{(1+\Gamma_j^2)+\frac{2\Gamma_j}{\sigma_j}\eta_j^{\mathrm{U}}} \overset{\sigma_j \to 0}{\longrightarrow} \frac{\eta_j^{\mathrm{U}}}{1+|S_j|\eta_j^{\mathrm{U}}}, \ m \ge j > 1. \end{aligned} \tag{3.12}$$

These conditions can be derived by transferring the Robin-type relations of F and F' at material interfaces z_j by a single adjacent material layer to z_{j+1} (using the matrix $\boldsymbol{M}_{[j+1]}^{\dagger+}(\sigma_{j+1})$ from Equation (3.9), obtaining the following η_{j+2}^{L}) or z_{j-1} (using $\boldsymbol{M}_{[j]}^{\dagger-}(\sigma_j)$, obtaining η_{j-1}^{U}). When $\Gamma_j \approx 1$, the expressions at both sides of the equations are also small, and we avoid undesired additions and subtractions of small and moderate numbers in this formula.

Remark 4. The procedures of Remark 3 can also be used for Dirichlet BCs, $F(0) = F(Z) = 0$ (e.g., $\rho = 0$ in BCs (2.7)). The procedure (3.12) should be started from $\left[\eta_2^{\mathrm{L}} - \sigma_1\right] = \frac{\sigma_1(1-\Gamma_1)^2}{2\Gamma_1}$ and $\left[\eta_{m-1}^{\mathrm{U}} - \sigma_m\right] = \frac{\sigma_m(1-\Gamma_m)^2}{2\Gamma_m}$ in this case.

3.4 Helmholtz problem

The Helmholtz problem (2.5)–(2.7) defines the vertical mode $\Theta(z)$ and the effective index $n_\bullet$. To find $n_\bullet$, we look for the roots of the related characteristic equation [2, 4]. $\Theta(z)$ is reconstructed using transfer matrices.

Theorem 1. *The problem* (2.5)–(2.7) *with* $\rho \in \{0, 1\}$ *has a nontrivial solution* $\Theta(z) \in C^2(\cup_{j=1}^m S_j) \cup C^1([0, Z])$ *if and only if the characteristic equality*

$$0 = \chi(\sigma) \overset{def}{=} \begin{cases} \begin{pmatrix}\sigma_{\mathrm{U}} & 1\end{pmatrix} \boldsymbol{M}(Z, 0; \sigma) \begin{pmatrix}1 \\ \sigma_{\mathrm{L}}\end{pmatrix} & \text{if } \rho = 1 \quad \text{[Robin BC]}, \\ M_{12}(Z, 0; \sigma) & \text{if } \rho = 0 \quad \text{[Dirichlet BC]} \end{cases} \tag{3.13}$$

holds. Here (2×2)*-matrix* $\boldsymbol{M}(Z, 0; \sigma)$ *is constructed as suggested in Lemma 3.*

Proof. Let $\Theta(z)$ be a nontrivial solution to the considered problem. Assume that $\rho = 1$, s.t. $\Theta(0) \neq 0$. Otherwise, $\binom{\Theta}{\Theta'}$ vanishes at $z = 0$ due to BCs (2.7), at all material layer interfaces due to Lemma 3, and at the remaining z due to Lemma 2. The same consideration allows us to conclude that $\Theta(Z) \neq 0$ as well. Translation of the nontrivial $\binom{\Theta}{\Theta'}(0)$ over $[0, Z]$ using $\boldsymbol{M}(Z, 0; \sigma)$ and applying BCs (2.7) to eliminate $\Theta'(0)$ and $\Theta'(Z)$ from the resulting relation implies

the condition $\binom{1}{-\sigma_U}\Theta(Z) = \boldsymbol{M}(Z,0;\sigma)\binom{1}{\sigma_L}\Theta(0)$, which, after the multiplication of both sides by the row-vector $(\sigma_U\ 1)$ from the left gives characteristic equation (3.13). Assume now that $\chi(\sigma) = 0$, i.e.,

$$-\sigma_U[M_{11}(Z,0;\sigma) + \sigma_L M_{12}(Z,0;\sigma)] = M_{21}(Z,0;\sigma) + \sigma_L M_{22}(Z,0;\sigma).$$

Let us translate a vector $\binom{1}{\sigma_L}$ (satisfying BCs (2.7) at $z = 0$) with $\boldsymbol{M}(z,0;\sigma)$ over $[0,Z]$, obtaining nontrivial $\Theta(z)$ and $\Theta'(z)$ in this way. Within $[0,Z]$, $\Theta(z)$ solves Equations (2.5), (2.6). At $z = Z$, $\binom{\Theta}{\Theta'}(Z) = \boldsymbol{M}(Z,0;\sigma)\binom{1}{\sigma_L} \propto \binom{1}{-\sigma_U}$, i.e., $\Theta(z)$ satisfies BCs (2.7) at $z = Z$ and, thus, solves our problem.

For $\rho = 0$, the BCs (2.7) are of Dirichlet-type, such that a nontrivial $\Theta(z)$ should have non-vanishing $\Theta'(0)$ and $\Theta'(Z)$. Translation of $\binom{0}{\Theta'(0)}$ over $[0,Z]$ implies $\binom{0}{1}\Theta'(Z) = \boldsymbol{M}(Z,0;\sigma)\binom{0}{1}\Theta'(0)$, which gives us $\chi(\sigma) = 0$ in (3.13). On the other hand, if $\chi(\sigma) = 0$, by propagating $\binom{\Theta}{\Theta'}(0) = \binom{0}{1}$ over $[0,Z]$, we obtain a nontrivial $\Theta(z)$ solving Equations (2.5), (2.6), and at $z = Z$ satisfying the relation $\Theta(Z) = \chi(\sigma)$, i.e., fulfilling Dirichlet BCs in (2.7). □

Corollary 4. Matrix $\boldsymbol{M}(Z,0;\sigma)$ in Equation (3.13) can be replaced by $\boldsymbol{M}^{\dagger+}_{[m,0]}(\sigma)$ or by another matrix $\boldsymbol{M}^{\dagger\dagger+}_{[m,0]}(\sigma)$ obtained after substituting $\boldsymbol{M}^{\dagger+}_{[j]}(\sigma_j)$ within some layers S_j in Equation (3.9) with the original layer-wise propagator $\boldsymbol{M}_j(z_j, z_{j-1}; \sigma_j)$.

Proof. The proof is identical to that of Theorem 1, since, due to Corollary 3, $\boldsymbol{M}^{\dagger+}_{[m,0]}(\sigma)$ or $\boldsymbol{M}^{\dagger\dagger+}_{[m,0]}(\sigma)$ can be obtained from $\boldsymbol{M}(Z,0;\sigma)$ by multiplying it with a non-vanishing factor composed of all or several multipliers $e^{-\sigma_j|S_j|}$. □

4 Construction of the coupling matrix $\boldsymbol{C}$

Notations and statements presented in the previous section are used for constructing the field coupling matrix $\boldsymbol{C}$, which will be discussed in this section.

4.1 Vertical mode and its intensity

According to Theorem 1 and Corollary 4, Equation (3.13) can be written as

$$\chi(n_\bullet) \stackrel{def}{=} \chi(\tilde{\sigma}(n_\bullet, n(z))) = 0, \tag{4.1}$$

where $\tilde{\sigma}$ is defined in Equation (2.5), and $n(z)$ is a layer-wise constant positive real function introduced in Subsection 2.2. Since $n(z)$ is real, all physically relevant $n_\bullet$ satisfying Equation (2.6) and, thus, Equation (3.13) are also real and belong to the interval $(0, \max_z n(z)]$. To find these roots, we scan $\chi(\xi)$ along the suggested interval, detect rough approximations of $n_\bullet$, and correct them using the Newton-Raphson iterative procedure, exploring analytic expressions for χ and χ'. We construct the characteristic function (4.1) using the matrix $\boldsymbol{M}^{\dagger+}_{[m,0]}(\sigma)$ (3.9). The layer-wise constant $\sigma(z)$ is defined by the parameters σ_L, σ_U, and σ_r, $r = 1,\dots,m$, which are functions of the variable ξ in (2.5). Accounting that $\frac{d}{d\xi}\sigma_\nu(\xi) = \frac{k_0^2\xi}{\sigma_\nu(\xi)}$, we can construct the function

$\chi(\tilde\sigma(\xi,n(z))) = \chi(\xi)$ and its ξ-derivative using the recurrent matrix-vector multiplication procedure:

$$\chi(\xi) = \binom{\sigma_{\mathrm{U}}}{1}^T \mathcal{F}_m(\xi),\ \chi'(\xi) = \binom{\sigma_{\mathrm{U}}}{1}^T \mathcal{F}'_m(\xi) + \tfrac{k_0^2\xi}{\sigma_{\mathrm{U}}}\binom{1}{0}^T \mathcal{F}_m(\xi), \quad \text{where}$$
$$\begin{cases} \mathcal{F}_r(\xi) \overset{def}{=} \boldsymbol{M}^{\dagger+}_{[r]}(\sigma_r)\mathcal{F}_{r-1}(\xi), \\ \mathcal{F}'_r(\xi) \overset{def}{=} \boldsymbol{M}^{\dagger+}_{[r]}(\sigma_r)\mathcal{F}'_{r-1}(\zeta) + \frac{k_0^2\xi \frac{d}{d\sigma}\boldsymbol{M}^{\dagger+}_{[r]}(\sigma_r)}{\sigma_r}\mathcal{F}_{r-1}(\xi), \end{cases} \quad 1 \le r \le m,$$
$$\mathcal{F}_0(\xi) = \binom{1}{\sigma_{\mathrm{L}}}, \quad \mathcal{F}'_0(\xi) = \left[\tfrac{d}{d\sigma_{\mathrm{L}}}\binom{1}{\sigma_{\mathrm{L}}}\right]\tfrac{d\sigma_{\mathrm{L}}}{d\xi} = \tfrac{k_0^2\xi}{\sigma_{\mathrm{L}}}\binom{0}{1}.$$

If $\sigma_j(\xi) \to 0$, factor $\mathcal{F}'_j(\xi)$ is undefined. Thus, following the statement of Corollary 4, for those layers where $|e^{|S_j|\sigma_j(\xi)}|$ remains moderate (1 for $\sigma_j = 0$), during the construction of $\chi(\xi)$ instead of $\boldsymbol{M}^{\dagger+}_{[j]}(\sigma_j)$, one should better use $\boldsymbol{M}_j(z_j, z_{j-1}; \sigma_j)$, which has a well-defined ξ-derivative even for vanishing σ_j:

$$\frac{d}{d\xi}\boldsymbol{M}_j(z_j, z_{j-1}; \sigma_j(\xi)) = \frac{k_0^2\xi\frac{d}{d\sigma}\boldsymbol{M}_j(z_j, z_{j-1}; \sigma_j)}{\sigma_j} \overset{\sigma_j\to 0}{\longrightarrow} k_0^2\xi|S_j|\begin{pmatrix} |S_j| & \frac{|S_j|^2}{3} \\ 2 & |S_j| \end{pmatrix}.$$

After finding vertical-mode-defining $n_\bullet$, we reconstruct the vertical mode and find its layer-wise intensities $\mathcal{P}_j^{\Theta}$ using the following steps:

i) Find $\sigma_j = \tilde\sigma(n_\bullet, n_j)$, $1 \le j \le m$ (and $j \in \{\mathrm{L}, \mathrm{U}\}$, if $\rho = 1$ in Equation (2.7));

ii) Find factors η^{L} (or η^{U}) for Robin-type relations of Θ and Θ' (3.11) at the border z_k of the active zone or PC layer (where $|\Theta|$ is expected to be large) using Remark 3 (and Remark 4, if Dirichlet BCs are considered);

iii) Set $\binom{\Theta_u}{\Theta'_u}(z_k) = \binom{1}{\eta^{\mathrm{L}}_{k+1}}$ and propagate this vector towards $z = Z$ and $z = 0$ with transfer matrices (3.8) and (3.6). The selection of z_k allows us to avoid large exponential growth within the layers S_j with large $\Re\sigma_j|S_j|$. Here, we can have less vital exponential decay towards zero instead;

iv) During propagation, collect $\Theta_u(z)$ at the layer borders and use them to evaluate the mode power $\mathcal{P}_j^{\Theta_u}$ in each layer S_j; see Equations (2.10) and (3.7) for the definition of matrix $\boldsymbol{p}_j$. For Robin BCs, we have $\Theta_u(\pm\infty) = 0$ and $\Gamma_{0,m+1} \to 1$, s. t. in the infinitely long outside regions S_0 and S_{m+1} the relations $\mathcal{P}_0^{\Theta_u} = |\Theta_u(0)|^2/(2\sigma_{\mathrm{L}})$ and $\mathcal{P}_{m+1}^{\Theta_u} = |\Theta_u(Z)|^2/(2\sigma_{\mathrm{U}})$ hold;

v) $\mathcal{P}_T^{\Theta_u} = \sum_{j=0}^{m+1}\mathcal{P}_j^{\Theta_u}$ is the overall intensity of the unscaled mode $\Theta_u(z)$. It is used for the final mode scaling, $\Theta(z) = \Theta_u(z)/(\mathcal{P}_T^{\Theta_u})^{1/2}$, and for defining the scaled mode power within the layers, $\mathcal{P}_j^{\Theta} = \mathcal{P}_j^{\Theta_u}/\mathcal{P}_T^{\Theta_u}$.

An example with six calculated vertical modes and corresponding function $n(z)$ is shown in Figure 2. We used vertical structure and the cell size a from [6] and Robin BCs with $n_{\mathrm{L}} = n_{\mathrm{U}} = 1$ in calculations. PC cells contain two air-filled 45° slanted ellipses centered at $(x_\pm, y_\pm) = (\pm\frac{a}{8}, \pm\frac{a}{8})$, see the middle diagram of Figure 1(d), implying $n_\bullet \approx 3.429$ [6]. Besides the broad n- and p-cladding

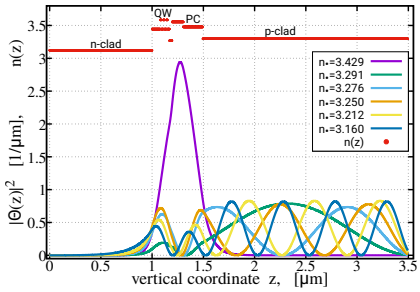

Figure 2. Six calculated scaled vertical modes (solid lines) and corresponding function $n(z)$ (red dots). Magenta: the main mode used for construction of $\boldsymbol{C}$.

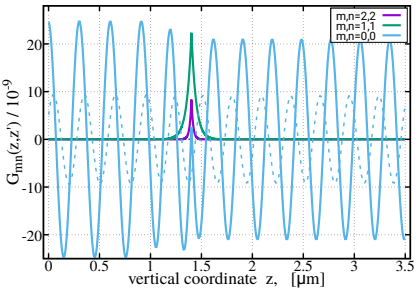

Figure 3. Green's functions $G_{(0,0)}$ (magenta), $G_{(1,1)}$ (green), and $G_{(2,2)}$ (light blue) at fixed z' within the PC layer. Solid and dashed: real and imaginary parts of G_p.

layers at the edges of Figure 2, we distinguish an active region composed of three quantum wells (QWs) and a PC layer. The mode with the largest $n_\bullet$ and largest intensity within the QW layer is the vertical mode of our interest.

4.2 Green's function and related integral expressions

When reconstructing $G_p(z,z')$ [8] for $(z,z') \in S_k \times S_j$, we distinguish the cases of $k=j$ and $k \neq j$. In the first case, for $z \in \cup_{l=1}^{j-1} S_l$ or $z \in \cup_{l=j+1}^{m} S_l$ and $z' \in S_j$, Equations (2.11), (2.12) are similar to (3.3), (3.10). We use matrices $\boldsymbol{M}^\dagger$ and Remark 3 to calculate $\eta_{p,j}^{\mathrm{L}}$ and $\eta_{p,j}^{\mathrm{U}}$, determining Robin BCs (3.11) at the edges of S_j. In subregions $z<z'$ and $z>z'$ of the square $S_j \times S_j$, the Green's functions solve the homogeneous Equation (2.11), i.e., they can be written as[3]

$$G_p(z,z') = \begin{cases} B_{p,j}^{L+}(z')e^{\sigma_{p,j}z} + B_{p,j}^{L-}(z')e^{-\sigma_{p,j}z} & \text{for } z<z', \\ B_{p,j}^{U+}(z')e^{\sigma_{p,j}z} + B_{p,j}^{U-}(z')e^{-\sigma_{p,j}z} & \text{for } z>z. \end{cases}$$

$G_p(z,z')$ satisfies BCs (3.11) at $z=z_{j-1}$ and z_j and the connection conditions (2.13) at $z=z'$. By resolving the resulting system of four inhomogeneous equations w.r.t. four variables $B_{p,j}^{L\pm}$, $B_{p,j}^{U\pm}$, we can rewrite $G_p(z,z')$ as

$$\begin{aligned} G_p(z,z') &= \frac{e^{-\sigma_{p,j}|z-z'|}}{2\sigma_{p,j}} + \mathcal{E}_{p,j}^T(z')\boldsymbol{B}_{p,j}\mathcal{E}_{p,j}(z), \quad \text{where} \\ \mathcal{E}_{p,j}(\xi) &= (1+\Gamma_{p,j}) \begin{pmatrix} e^{\sigma_{p,j}(\xi-z_j)} \\ e^{\sigma_{p,j}(z_{j-1}-\xi)} \end{pmatrix}, \\ \boldsymbol{B}_{p,j} &= \begin{pmatrix} \frac{(\sigma_{p,j}+\eta_{p,j}^{\mathrm{L}})(\sigma_{p,j}-\eta_{p,j}^{\mathrm{U}})}{2\sigma_{p,j}\Delta_{p,j}} & \frac{(\sigma_{p,j}-\eta_{p,j}^{\mathrm{L}})(\sigma_{p,j}-\eta_{p,j}^{\mathrm{U}})(1-\Gamma_{p,j})}{2\sigma_{p,j}\Delta_{p,j}(1+\Gamma_{p,j})} \\ \frac{(\sigma_{p,j}-\eta_{p,j}^{\mathrm{L}})(\sigma_{p,j}-\eta_{p,j}^{\mathrm{U}})(1-\Gamma_{p,j})}{2\sigma_{p,j}\Delta_{p,j}(1+\Gamma_{p,j})} & \frac{(\sigma_{p,j}-\eta_{p,j}^{\mathrm{L}})(\sigma_{p,j}+\eta_{p,j}^{\mathrm{U}})}{2\sigma_{p,j}\Delta_{p,j}} \end{pmatrix}, \\ \Delta_{p,j} &= (\sigma_{p,j}+\eta_{p,j}^{\mathrm{L}})(\sigma_{p,j}+\eta_{p,j}^{\mathrm{U}})(1+\Gamma_{p,j})^2 \\ &\quad -(\sigma_{p,j}-\eta_{p,j}^{\mathrm{L}})(\sigma_{p,j}-\eta_{p,j}^{\mathrm{U}})(1-\Gamma_{p,j})^2. \end{aligned} \tag{4.2}$$

[3] Note that $|p| \neq 1$, such that $|\sigma_{p,j}|$ is not vanishing.

Inspired by the form of $G_p(z,z')$ within $S_j\times S_j$, given as a linear combination of four exponentials $e^{\nu\sigma_{p,j}z}e^{\nu'\sigma_{p,j}z'}$, $\{\nu,\nu'\}\in\{\pm\}$, we seek to write G_p for any $z'\in S_j$ and z belonging to any of material interfaces, $z=z_l$, $0<l<m$, as

$$G_p(z_l,z')=(\mathcal{J}^j_{p,l})^T\mathcal{E}_{p,j}(z'),\quad \text{with } z'\text{-independent }\ \mathcal{J}^j_{p,l}=\begin{pmatrix}\mathcal{J}^{j+}_{p,l}\\ \mathcal{J}^{j-}_{p,l}\end{pmatrix}. \tag{4.3}$$

Indeed, at both sides of the S_j-layer, Equation (4.2) provides the relations

$$\mathcal{J}^{j\pm}_{p,j-1}=\tfrac{(1\mp\Gamma_{p,j})(\sigma_{p,j}\mp\eta^{\mathrm{U}}_{p,j})}{\Delta_{p,j}},\quad \mathcal{J}^{j\pm}_{p,j}=\tfrac{(1\pm\Gamma_{p,j})(\sigma_{p,j}\pm\eta^{\mathrm{L}}_{p,j})}{\Delta_{p,j}}. \tag{4.4}$$

Since $z'\in S_j$, Green's function defining Equation (2.11) is homogeneous for $z\le z_{j-1}$ and $z\ge z_j$. Due to Lemma 3 and Corollary 3, one can translate $\binom{G_p}{\partial_z G_p}(z,z')$ from z_{j-1} to z_l, $l<j-1$, and z_j to z_l, $l>j$, using $\boldsymbol{M}^{\dagger-}_{[l]}(\sigma_{p.l})$ and $\boldsymbol{M}^{\dagger+}_{[l]}(\sigma_{p.l})$ (3.9), respectively. Exploiting the relations $\partial_z G_p(z_l,z')=\eta^{\mathrm{L}}_{p,l+1}G_p(z_l,z')$, $l<j$, and $\partial_z G_p(z_l,z')=-\eta^{\mathrm{U}}_{p,l}G_p(z_l,z')$, $l\ge j$, with η^{L} and η^{U} derived following Remark 3 and collecting the terms at the corresponding exponentials $e^{\pm\sigma_{p,l}(z'-\bar z_l)}$ provide the required relations

$$\begin{aligned}\mathcal{J}^{j\pm}_{p,l-1}&=\tfrac{\sigma_{p,l}(1-\Gamma^2_{p,l})}{\sigma_{p,l}(1+\Gamma^2_{p,l})+2\eta^{\mathrm{L}}_{p,l}\Gamma_{p,l}}\mathcal{J}^{j\pm}_{p,l},\quad l=j-1,\dots,1,\\ \mathcal{J}^{j\pm}_{p,l}&=\tfrac{\sigma_{p,l}(1-\Gamma^2_{p,l})}{\sigma_{p,l}(1+\Gamma^2_{p,l})+2\eta^{\mathrm{U}}_{p,l}\Gamma_{p,l}}\mathcal{J}^{j\pm}_{p,l-1},\quad l=j+1,\dots,m.\end{aligned} \tag{4.5}$$

For any $k\ne j$ and $z\in S_k$, parametrically on $z'\in S_j$ depending $G_p(z,z')$ satisfies homogeneous equation (3.3) and, thus, is defined by the analog of Equation (3.5) with boundary values $\mathcal{B}^{G_p(\cdot,z')}_k$ (i.e., $G_p(z_{k-1},z')$ and $G_p(z_k,z')$) given by Equations (4.3)–(4.5) and $\theta_{p,k}(z)$ defined using $\sigma_{p,k}$ instead of σ_k. One can show that in each subregion $S_k\times S_j$, $k\ne j$, $G_p(z,z')$ can be written as

$$\begin{aligned}&G_p(z,z')=\mathcal{E}^T_{p,j}(z')\boldsymbol{A}^j_{p,k}\mathcal{E}_{p,k}(z),\qquad \text{where}\\ &\boldsymbol{A}^j_{p,k}=\begin{cases}A^{\dagger j}_{p,k}\mathcal{J}^j_{p,k}\begin{pmatrix}(1+\Gamma_{p,k})(\sigma_{p,k}+\eta^{\mathrm{L}}_{p,k})\\ (1-\Gamma_{p,k})(\sigma_{p,k}-\eta^{\mathrm{L}}_{p,k})\end{pmatrix}^T & \text{if } k<j,\\ A^{\dagger j}_{p,k}\mathcal{J}^j_{p,k-1}\begin{pmatrix}(1-\Gamma_{p,k})(\sigma_{p,k}-\eta^{\mathrm{U}}_{p,k})\\ (1+\Gamma_{p,k})(\sigma_{p,k}+\eta^{\mathrm{U}}_{p,k})\end{pmatrix}^T & \text{if } k>j,\end{cases}\\ &A^{\dagger j}_{p,k}=\tfrac{1}{2(1+\Gamma^2_{p,k})\sigma_{p,k}+2\Gamma_{p,k}\left[(\eta^{\mathrm{L}}_{p,k}+\eta^{\mathrm{U}}_{p,k})-\operatorname{sgn}(k-j)(\eta^{\mathrm{L}}_{p,k}-\eta^{\mathrm{U}}_{p,k})\right]}.\end{aligned} \tag{4.6}$$

Examples of three Green's functions $G_p(z,z')$ for $p=(0,0)$, $(1,1)$, and $(2,2)$ for the fixed z' and the parameters explored in Figure 2 are shown in Figure 3. For $|p|=0$, the function has non-vanishing and, within each but z'-containing layer, harmonically oscillating real and imaginary parts. For other p, $\Im G_p=0$, whereas $\Re G_p$ has a sharp exponentially growing/decaying spike at $z=z'$. This shape of G_p suggests that for large $|p|$, a fully numerical estimation of $\mathcal{G}_p$ requires fine numerical meshes and considerable computational time.

Let us switch to calculating matrices $\boldsymbol{g}^{(k,j)}_p$ from Equation (2.10). For contributions due to continuously differentiable part of G_p (defined by matrices

$\boldsymbol{B}$ and $\boldsymbol{A}$ in Equations (4.2), (4.6)), separation of variables z and z' is possible, and we only need to calculate layer-wise integrals of the matrix-function $\theta_j(z)\mathcal{E}^T_{p,j}(z)$, with $\mathcal{E}_{p,j}$ and θ_j defined in Equations (4.2) and (3.5), respectively:

$$\int_{S_j}\theta_j(z)\mathcal{E}^T_{p,j}(z)dz=\boldsymbol{I}_{p,j}=\begin{pmatrix} I^+_{p,j} & I^-_{p,j}\\ I^-_{p,j} & I^+_{p,j}\end{pmatrix},\qquad \text{where}$$
$$I^{\pm}_{p,j}=\frac{(\sigma_{p,j}\mp\sigma_j\Gamma_j)(\Gamma_{p,j}\pm1)\mp\frac{\sigma_j}{\Gamma_j}(1-\Gamma_j^2)\Gamma_{p,j}}{(\sigma^2_{p,j}-\sigma^2_j)}\overset{\sigma_j\to0}{\longrightarrow}\frac{\sigma_{p,j}|S_j|(\Gamma_{p,j}\pm1)\mp2\Gamma_{p,j}}{\sigma^2_{p,j}|S_j|}.$$

The least trivial is the major contribution to $\boldsymbol{g}^{(j,j)}_p$, which involves double-integration of $e^{-\sigma_j|z-z'|}$ over $S_j\times S_j$ and requires splitting the inner integration region into two subintervals $[z_{j-1},z]$ and $[z,z_j]$. Still, we can show that

$$\int\limits_{S_j}\int\limits_{S_j}\theta_j(z')\,\tfrac{e^{-\sigma_{p,j}|z-z'|}}{2\sigma_{p,j}}dz'\,\theta^T_j(z)dz=\frac{\boldsymbol{p}_j}{(\sigma^2_{p,j}-\sigma^2_j)}-\boldsymbol{I}_{p,j}\boldsymbol{R}_{p,j}\boldsymbol{I}_{p,j},\ \text{where}$$
$$\boldsymbol{R}_{p,j}=R^{\dagger}_{p,j}\begin{pmatrix}R'_{p,j} & R''_{p,j}\\ R''_{p,j} & R'_{p,j}\end{pmatrix},\qquad R'_{p,j}=\frac{(\sigma^2_{p,j}-\sigma^2_j)}{\sigma_{p,j}(1+\Gamma_j)}\overset{\sigma_j\to0}{\longrightarrow}\sigma_{p,j},$$
$$R''_{p,j}=\frac{(\sigma^2_{p,j}+\sigma^2_j)(1-\Gamma_{p,j})+2\frac{\sigma_j}{\Gamma_j}\sigma_{p,j}(\Gamma_j^2-\Gamma_{p,j})}{\sigma_{p,j}(1+\Gamma_j)(1+\Gamma_{p,j})}\overset{\sigma_j\to0}{\longrightarrow}\frac{(1-\Gamma_{p,j})\sigma_{p,j}|S_j|-4\Gamma_{p,j}}{(1+\Gamma_{p,j})|S_j|},$$
$$R^{\dagger}_{p,j}=\frac{(1+\Gamma_j)}{8\big(\sigma_{p,j}-\frac{\sigma_j}{\Gamma_j}\Gamma_{p,j}\big)\big(\sigma_{p,j}\Gamma_{p,j}-\sigma_j\Gamma_j\big)}\overset{\sigma_j\to0}{\longrightarrow}\frac{|S_j|}{8\Gamma_{p,j}\sigma_{p,j}(\sigma_{p,j}|S_j|-2\Gamma_{p,j})}.$$

The expressions for $\boldsymbol{g}^{(k,j)}_p$ now can be written as

$$\boldsymbol{g}^{(k,j)}_p=\begin{cases}\frac{\boldsymbol{p}_j}{(\sigma^2_{p,j}-\sigma^2_j)}+\boldsymbol{I}_{p,j}[\boldsymbol{B}_{p,j}-\boldsymbol{R}_{p,j}]\boldsymbol{I}_{p,j} & \text{if } k=j,\\ \boldsymbol{I}_{p,j}\boldsymbol{A}^j_{p,k}\boldsymbol{I}_{p,k} & \text{if } k\neq j.\end{cases}$$

Recall that $\sigma_{p,j}$ is non-vanishing, $\sigma_{p,j}$ and $\eta^{\mathrm{L}}_{p,j}$ or $\eta^{\mathrm{U}}_{p,j}$ can be similar (corresponding differences are small), and, especially for large $|p|$, factor $\Gamma_{p,l}\approx1$, which should be ever accounted for when estimating the required expressions. All formulas in this subsection are written avoiding summations of numbers differing by many orders and divisions of very small or very large numbers. Such operations, used in sometimes more compact formulas for $\mathcal{P}^{\Theta}_j$ and $\mathcal{G}^{(k,j)}_{(r,s)}$, have led to inaccuracies of computer arithmetics and violations of calculations in our first version of the numerical code.

4.3 Truncation of the coupling matrix

As it was indicated in Equation (2.14), $\boldsymbol{C}$, or, more precisely, $\boldsymbol{C}_{2D}$, relies on the infinite sum of submatrices $\boldsymbol{C}^{(r,s)}_{2D}$, depending on the Fourier coefficients $\xi^j_{r\pm1,s}$, $\xi^j_{r,s\pm1}$ (2.9) and integral parameters $\mathcal{P}^{\Theta}_j$, $\mathcal{G}^{(k,j)}_{(r,s)}$ (2.10) with integration performed in the PC sublayer-defined regions. By the finite (truncated) sum

$$\boldsymbol{C}^{(M)}_{2D}=\textstyle\sum_{|r|+|s|>1,\{|r|,|s|\}\le M}\boldsymbol{C}^{(r,s)}_{2D},\tag{4.7}$$

we denote approximations of $\boldsymbol{C}_{2D}$ obtained using the truncation parameter M. The Fourier coefficients $\xi^j_{r,s}$ are obtained using the Fast Fourier Transform (FFT) of the uniformly in the unit cell of the PC discretized function

$\bar{n}^2(x,y,z)|_{z\in S_j}$. Thus, calculations of $\boldsymbol{C}_{2D}^{(M)}$ are only possible if the number of discretization steps along the cell sides more than twice exceeds the parameter M. In the calculation examples of Figure 4, we used the model parameters as in Figures 2 and 3 and a uniform $2^{11}\times 2^{11}$ discretization of the unit cell, which is sufficient for construction of the truncated sums with up to $M = 1022$.

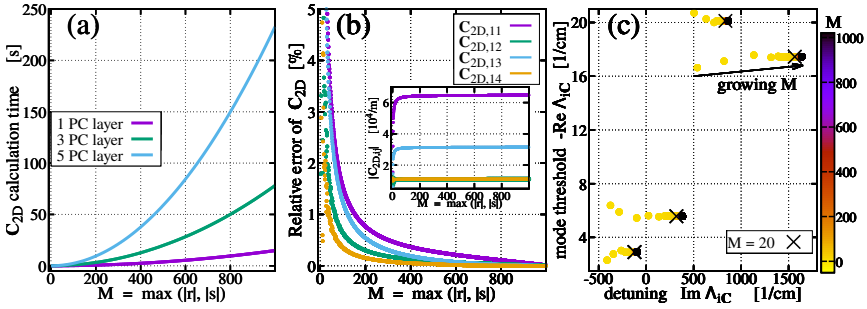

Figure 4. Calculations of $\boldsymbol{C}_{2D}^{(M)}$ in dependence on the truncation parameter M (4.7). (a): Time required for calculations of $\boldsymbol{C}_{2D}^{(M)}$ in the same PCSEL with 1, 3, and 5 PC layers. (b): Relative error of $\boldsymbol{C}_{2D}^{(M)}$ elements as function of M. Inset: moduli of these elements. (c): Spectrum of $i\boldsymbol{C}$ in dependence on M. X: eigenvalues of $i\boldsymbol{C}$ obtained using $\boldsymbol{C}_{2D}^{(20)}$.

In Figure 4(a), we show the time needed for calculations of $\boldsymbol{C}_{2D}^{(M)}$ with different M when the PCSEL has a single PC layer (magenta) or this layer is subdivided into three (green) and five (light blue) sublayers, respectively. With an increase of M, this time grows quadratically in all three cases, which is in accord with a quadratic growth of the parameter set $\{(r,s)\}$ satisfying the summation conditions in Equation (4.7). An increase in the number of PC sublayers implies another, approximately quadratic, growth of the calculation time, which is due to the necessity of estimating factors $\mathcal{G}_p^{(k,j)}$ for growing sets of PC layer indices $\{(k,j)\}$ (recall that in the structure with a single PC layer S_k, a single factor $\mathcal{G}_p^{(k,k)}$ is needed for each value of $|p|$). We note that Figure 4(a) shows only the time needed for the estimation of $\boldsymbol{C}_{2D}^{(M)}$. Time spent for construction of the whole matrix $\boldsymbol{C}$ using $M = 1020$ (including reading and preprocessing of model parameters, 2-dimensional FFT of $\bar{n}(x,y,z)$, and finding the vertical mode and the remaining components of $\boldsymbol{C}$) was about 41, 107, and 268 s in 1-, 3-, and 5-PC-layer cases, respectively. In contrast to the above-used analytic formulas, calculations of $\boldsymbol{C}$ using $M = 20$, multi-layer PCs, and fully numerical procedures for integral factors $\mathcal{G}_p^{(k,j)}$ and $\mathcal{P}_j^{\Theta}$ took the whole day and even more.

Figure 4(b) shows the evolution of the relative error $|(\boldsymbol{C}_{2D,ij}^{(M)}-\boldsymbol{C}_{2D,ij})/\boldsymbol{C}_{2D,ij}|$ (main diagram, $\boldsymbol{C}_{2D}^{(1020)}$ was used instead of the exact $\boldsymbol{C}_{2D}$) and $|\boldsymbol{C}_{2D,ij}^{(M)}|$ (insert) with an increase of M. Since $\boldsymbol{C}_{2D}$ is Hermitian [6,7] and due to the symmetry of the PC cell w.r.t. $y = x$ line, the moduli of all $\boldsymbol{C}_{2D}$ components are represented by these four curves. Notably, $M = 160$ is sufficient to reduce the relative errors of all $\boldsymbol{C}_{2D}$ elements to 1% and less in this case. In practical calculations, where estimation of the eigenvalues of the spectral problem (2.3) is required, even

smaller values of M can be sufficient. The illustration is given in Figure 4(c), showing changes in the spectra of $i\boldsymbol{C}$ calculated using truncated $\boldsymbol{C}_{2D}^{(M)}$ with an increase of M. Crosses in this diagram, representing the eigenvalues $\Lambda_{i\mathbf{C}}$ obtained with a moderate $M = 20$, have nearly the same real parts and not so much distinguishable imaginary parts as the eigenvalues calculated using high M (dark bullets in the same figure). Since $\Lambda_{i\mathbf{C}}$ give us decent approximations of the eigenvalues solving Equation (2.3) with $L \to \infty$, we expect that moderate M can be sufficient when considering the same problem for large but still finite L.

5 Numerical solution of the spectral problem

Similar spectral problems defined in one-dimensional domains occur, e.g., in the analysis of edge-emitting distributed-feedback lasers. Often, these problems can be solved exactly for a finite number of modes using transfer matrices, characteristic functions, and replacement of the spectral problem by the root-finding problem [10], as it was done in Subsection 4.1. In the limit case of fully decoupled cross-propagating field functions Φ_u and Φ_v, i.e., when off-diagonal 2×2 blocks of matrix $\boldsymbol{C}$ are $\mathbf{0}$, Equation (2.3) splits into a pair of effectively one-dimensional problems. As will be shown later in this work, exact eigenvalues Λ_{1D} for this limit-case problem can still provide reasonable approximations for certain eigenvalues of the whole system. To find the modes in the general case, we use a fully numerical approach based on finite difference approximations. To construct a numerical scheme, we subdivide the domain $[0, L] \times [0, L]$ into n^2 squares with the side length $h = \frac{L}{n}$, and introduce the staggered mesh,

$$\begin{aligned}&\omega_u^h = \omega_x'^h \times \omega_y''^h \qquad \text{and} \qquad \omega_v^h = \omega_x''^h \times \omega_y'^h, \qquad \text{where}\\ &\omega_\xi'^h = \{\xi_j = jh,\ 0 \le j \le n\}, \quad \omega_\xi''^h = \{\xi_{j-\frac{1}{2}} = (j-\tfrac{1}{2})h,\ 1 \le j \le n\},\end{aligned}$$

see black and red bullets in Figure 5. This mesh defines the $4n(n+1)$-component grid function Φ^h, which is used to approximate $\Phi(x, y)$ from Equation (2.2):

$$\begin{aligned}&\Phi^h = \begin{pmatrix}\Phi_u^h\\ \Phi_v^h\end{pmatrix}, \quad \Phi_u^h = \begin{pmatrix}\Phi_u^{h+}\\ \Phi_u^{h-}\end{pmatrix}, \quad \Phi_v^h = \begin{pmatrix}\Phi_v^{h+}\\ \Phi_v^{h-}\end{pmatrix}, \quad \text{where}\\ &\Phi_{u,j,l-0.5}^{h\pm} \approx \Phi_u^{\pm}(x_j, y_{l-0.5}), \quad \Phi_{v,j-0.5,l}^{h\pm} \approx \Phi_v^{\pm}(x_{j-0.5}, y_l).\end{aligned}$$

These components are variables of the linear system consisting of $4n^2$ equations approximating each of four equations in (2.3) at n^2 spatial positions $\omega_x''^h \times \omega_y''^h$ (central positions of small squares in Figure 5) and $4n$ BC-induced relations:

$$\begin{aligned}&\begin{pmatrix}\boldsymbol{\sigma}\partial_x^h & \mathbf{0}\\ \mathbf{0} & \boldsymbol{\sigma}\partial_y^h\end{pmatrix}\Phi^h = \big[i\boldsymbol{C} - \Lambda_h\big]\bar{\Phi}^h, \qquad (x, y) \in \omega_x''^h \times \omega_y''^h,\\ &\Phi_{u,0,k-0.5}^{h+} = \Phi_{u,n,k-0.5}^{h-} = \Phi_{v,k-0.5,0}^{h+} = \Phi_{v,k-0.5,n}^{h-} = 0, \quad 1 \le k \le n.\end{aligned} \tag{5.1}$$

Here, $\partial_x^h\Phi^h$, $\partial_y^h\Phi^h$, and $\bar{\Phi}^h$ are linear operators of the grid function Φ^h, providing finite-difference approximations of $\frac{\partial}{\partial x}\Phi$, $\frac{\partial}{\partial y}\Phi$, and Φ at $\omega_x''^h \times \omega_y''^h$.

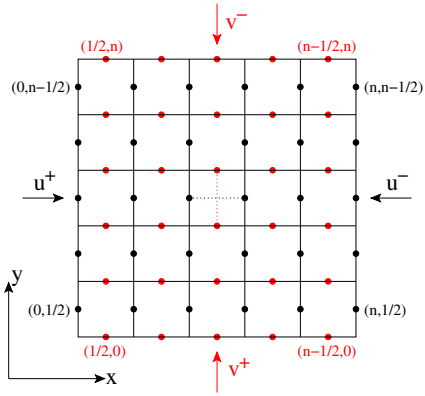

Figure 5. Scheme of the discretized computation domain. Bullets indicate spatial positions where mesh functions Φ_u^h and Φ_v^h are defined.

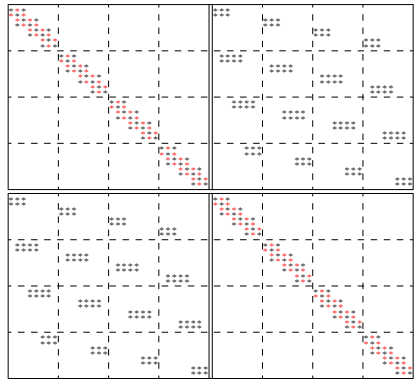

Figure 6. Schematics of sparse matrices $\boldsymbol{H}_h$ (non-vanishing black and red elements) and $\boldsymbol{D}_h$ (non-vanishing red elements) for the second order finite difference scheme.

5.1 Second order finite difference scheme

A simple approximation of Equations (2.3) at $\omega_x''^h \times \omega_y''^h$ is given by the second-order finite difference scheme (5.1), obtained using

$$\begin{aligned} \bar{\Phi}^{h\pm}_{u,j,l} &\stackrel{def}{=} \sigma_j^h \Phi^{h\pm}_{u,\cdot,l-0.5}, & \bar{\Phi}^{h\pm}_{v,j,l} &\stackrel{def}{=} \sigma_l^h \Phi^{h\pm}_{v,j-0.5,\cdot}, \\ \partial_x^h \Phi^{h\pm}_{u,j,l} &\stackrel{def}{=} \sigma_j^{\dagger h} \Phi^{h\pm}_{u,\cdot,l-0.5}, & \partial_y^h \Phi^{\pm}_{v,j,l} &\stackrel{def}{=} \sigma_l^{\dagger h} \Phi^{h\pm}_{v,j-0.5,\cdot}, \end{aligned} \tag{5.2}$$

where operators σ_k^h and $\sigma_k^{\dagger h}$ are given by

$$\sigma_k^h V^h = \tfrac{V_k^h + V_{k-1}^h}{2}, \qquad \sigma_k^{\dagger h} V^h = \tfrac{V_k^h - V_{k-1}^h}{h}, \qquad 1 \le k \le n. \tag{5.3}$$

A discrete analog of conservation law (2.4) holds for Equations (5.1)–(5.3), which indicates good quality of the numerical scheme.

Lemma 5. *Let Λ_h and nontrivial Φ^h satisfy Equations* (5.1)–(5.3). *Then*

$$\begin{aligned} &\mathcal{I}_g^h = \mathcal{I}_v^h + \mathcal{I}_l^h, \quad \textit{where} \quad \mathcal{I}_g^h = -2\Re\Lambda_h \left\|\bar{\Phi}^h\right\|_h^2, \ \mathcal{I}_v^h = 2\Im(\bar{\Phi}^h, \boldsymbol{C}_{\mathrm{rd}}\bar{\Phi}^h)_h, \\ &\mathcal{I}_l^h = h\sum_{j=1}^{n} |\Phi^{h+}_{u,n,j-0.5}|^2 + |\Phi^{h-}_{u,0,j-0.5}|^2 + |\Phi^{h+}_{v,j-0.5,n}|^2 + |\Phi^{h-}_{v,j-0.5,0}|^2. \end{aligned} \tag{5.4}$$

Here $\bar{\Phi}^h$ and $\boldsymbol{C}\bar{\Phi}^h$ are n^2-component sets of four-component vectors $\bar{\Phi}^h_{j,l}$ and $\boldsymbol{C}\bar{\Phi}^h_{j,l}$; $(\bar{\xi}^h, \bar{\zeta}^h)_h = h^2 \sum_{j,l=1}^n \bar{\xi}^{h*T}_{j,l} \bar{\zeta}^h_{j,l}$ and $\left\|\bar{\xi}^h\right\|_h = (\bar{\xi}^h, \bar{\xi}^h)_h^{1/2}$ are discrete analogs of scalar products and norms introduced in Lemma 1.

Proof. Linear equations in (5.1) can be interpreted as a n^2-component set of four-equation subsystems, each approximating Equation (2.3) at different positions of $\omega_x''^h \times \omega_y''^h$. By applying the discrete scalar product with respect

to this set and $2\bar{\Phi}^h$, taking the real part, and eliminating $4n$ boundary elements, we get $\mathcal{I}_l^h = 2\Re\big(\bar{\Phi}^h, i\boldsymbol{C}\bar{\Phi}^h\big)_h + \mathcal{I}_g^h$. As in Remark 1, the relation $2\Re\big(\bar{\Phi}^h, i\boldsymbol{C}\bar{\Phi}^h\big)_h = i\big(\bar{\Phi}^h, [\boldsymbol{C} - \boldsymbol{C}^{*T}]\bar{\Phi}^h\big)_h = \mathcal{I}_v^h$ immediately leads to the proof of this Lemma. □

Substituting the expressions (5.2), (5.3) into Equation (5.1), multiplying them by 2, and eliminating the BCs allow rewriting our schemes as a standard generalized spectral problem (or corresponding classical spectral problem):

$$\boldsymbol{H}_h W^h = \Lambda_h \boldsymbol{D}_h W^h \qquad \Leftrightarrow \qquad \boldsymbol{D}_h^{-1}\boldsymbol{H}_h W^h = \Lambda_h W^h. \tag{5.5}$$

Here, the $4n^2$-dimensional vector W^h contains all variables of Φ^h except for boundary elements from Equation (5.1). Complex non-Hermitian $\boldsymbol{H}_h$ and real-valued $\boldsymbol{D}_h$ are sparse $4n^2 \times 4n^2$-matrices with $\sim 32n^2$ and $\sim 8n^2$ non-vanishing elements each. For example, we can set

$$\begin{aligned} W^h_{2j-1+2n(l-1)} &= \Phi^{h-}_{u,j-1,l-0.5}, & W^h_{2j+2n(l-1)} &= \Phi^{h+}_{u,j,l-0.5}, \\ W^h_{2l-1+2n(j-1+n)} &= \Phi^{h-}_{v,j-0.5,l-1}, & W^h_{2l+2n(j-1+n)} &= \Phi^{h+}_{v,j-0.5,l}, \end{aligned}$$

such that matrices $\boldsymbol{H}_h$ and $\boldsymbol{D}_h$ have at least half of their non-vanishing elements concentrated close to the main diagonal; see schematic representation of these matrices in Figure 6 for the case of $n = 4$. In the matrix $\boldsymbol{H}_h$, only the elements denoted by black or red stars are non-vanishing. In the easily invertible matrix $\boldsymbol{D}_h$, the elements denoted by black stars vanish as well, whereas at the red star positions stands 1. Once the algorithm is constructed correctly, calculating both matrix-vector products $\boldsymbol{H}_h V^h$ and $\boldsymbol{D}_h V^h$ requires $\sim 44n^2$ arithmetic operations; estimating $\boldsymbol{D}_h^{-1} V^h$ with arbitrary $4n^2$-dimensional vector V^h can be done with $\sim 4n^2$ operations. Construction of the whole matrix $\boldsymbol{D}_h^{-1}\boldsymbol{H}_h$ with $\sim 8n^3$ non-vanishing entries also requires $\sim 4n^2$ operations.

5.2 Example

All formulas, algorithms, and schemes presented above were implemented in the solver, which is well suited for the calculation of several essential optical modes of the PCSEL and is extensively used for simulating new design concepts of all-semiconductor broad-emission-area PCSELs. The implementation of algorithms was performed using the Julia programming language (version 1.9) [3]; the spectra of Equation (5.5) have been calculated exploring the function "eigen()" available within the Julia's "LinearAlgebra" library and/or using additionally installed ARPACK library. The choice of programming environment will enable a simplified connection to other in-house available Julia-based solvers for the simulation of different semiconductor device aspects. The example calculations presented in Figure 7 were performed for the PCSEL device with $L = 300\,\mu$m (as considered in [6]), with the vertical structure and PC layer's configuration explored already when performing calculations for Figures 2–4. In this example, the modes (Λ_h, Φ^h) solve the discrete spectral problem (5.1) for several small-to-moderate discretization parameter n values.

The numerical scheme (5.1) has $4n^2$ (i.e., a finite number of) eigenvalues Λ_h and, thus, is not able to approximate all (an infinite number of) eigenvalues

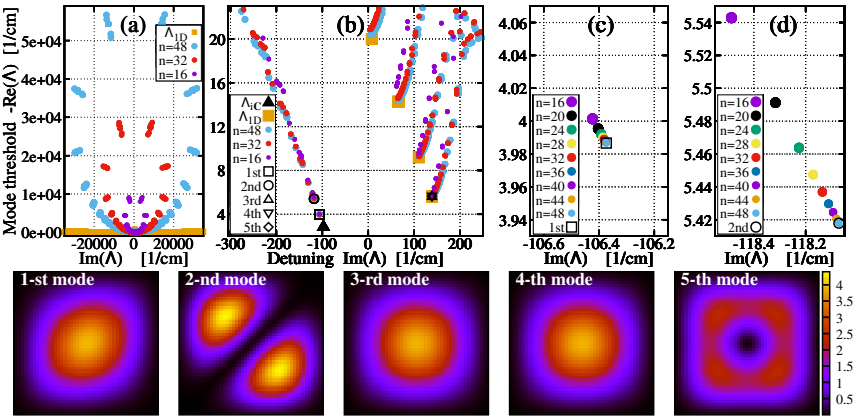

Figure 7. Calculations of eigenvalues Λ_h solving Equation (5.1). (a): All Λ_h for $n = 16$ (magenta), 32 (red), and 48 (light blue). (b): same Λ_h close to the origin. (c) and (d): Evolution of the main (smallest threshold) and the second mode with growing n. Empty symbols (squares, circles, triangles, rhombs) in (b)-(d): five main modes for $n = 48$. Orange full squares in (a), (b): eigenvalues Λ_{1D} in the limit case of the original system (2.3) with decoupled Φ_u and Φ_v. Black triangle in (b): lowest-threshold eigenvalue $\Lambda_{i\mathbf{C}}$. Bottom row: intensity distributions of five main eigenfunctions, $|\Phi^h(x, y)|^2$, within $[0, L] \times [0, L]$.

Λ of the original problem (2.3). Figure 7(a) shows how the spectra of (5.1) evolve with an increase of n. For each fixed n, most of Λ_h belong to the prolongated clusters, all grouped along a w.r.t. y-axis symmetric circle with a radius $\propto n = L/h$. Since $\boldsymbol{H}_h$ in Equation (5.5) is a complex non-Hermitian matrix, the spectra themself are not symmetric. The number of clusters and the number of modes within each cluster grows linearly with n. Eigenvalues with large $-\Re\Lambda_h$ are far away from realistic Λ, which for an uncoupled Φ_u and Φ_v case are represented by densely to each other located orange squares in panel (a). On the other hand, Λ_h with small $-\Re\Lambda_h$ and small or moderate $|\Im\Lambda_h|$ provide a much better resemblance of realistic Λ: see Figure 7(b) where only Λ_h within a small window close to the origin are shown. The closeness of $\Im\Lambda$ for the relevant modes to zero (where the numerical mode-circles are "flat") is guaranteed by the construction of the model equations, i.e., the choice of the central frequency (or the central wavelength λ_0). We can see four clusters of (red and light blue) modes with an accumulation of Λ_h close to four orange boxes, representing exact eigenvalues Λ_{1D} of Equation (2.3) with the decoupled cross-propagating fields. Note also that whereas the tips of two lower clusters of magenta modes (calculated for $n = 16$) are still well represented by Λ_{1D}, the remaining clusters are further apart, indicating an insufficient approximation of the corresponding modes at this low value of n.

Five main modes calculated with $n = 48$ are indicated by different empty black-framed symbols in the upper panels of Figure 7. Their intensity distributions $|\Phi^h(x, y)|^2 = |\Phi_u^{h+}|^2 + |\Phi_u^{h-}|^2 + |\Phi_v^{h+}|^2 + |\Phi_v^{h-}|^2$ are presented in the bottom-row panels. Notably, the total mode intensity $|\Phi(x, y)|^2$ incorporates spatial distributions of four complex components of the vector-eigenfunction

$\Phi(x,y)$, and the spectral problem (2.3) can have four modes with a single-lobed intensity pattern (fundamental band-edge modes, see, e.g., [7]), as the 1st, 3rd, and 4th modes in Figure 7. While third-to-fifth low-threshold modes are close to the lowest Λ_{1D} in Figure 7(b), two main modes belong to the mode group tending towards the filled black triangle, representing one of four eigenvalues $\Lambda_{i\boldsymbol{C}}$ of the matrix $i\boldsymbol{C}$ shown in Figure 2(c). It is a strong coupling of the cross-propagating fields, which implies a significant separation of these two most important modes from Λ_{1D}. The considered PCSEL configuration has a well-pronounced threshold gap between these two main modes. Moreover, the evolution of Λ_h of these modes with an increase of n, see Figure 7(c) and (d), lets us assume that already small $n \sim 20$ can provide pretty good approximations for several critical eigenvalues Λ of the original problem (2.3). More details on the convergence of these modes are provided in the following subsection.

The sufficiency of low n would be a perfect message in practical computations since calculations of all Λ_h for $n = 20$ took about 2 minutes, while the same task using $n = 40$ was performed in more than 4 hours. Finally, we note that in the presented example we still used a moderate value of L suggested in [6]. However, our algorithms also work well for much larger structures with $L > 1000\,\mu$m, which will be considered when designing new PCSEL devices.

5.3 Higher order schemes

When calculating the main modes with not so far from origin located $\Im\Lambda$, the schemes introduced above should provide a second-order approximation w.r.t. the discretization step h. Indeed, magenta curves in Figures 8(b) and (c) represent errors estimated for two main eigenvalues of the considered system decaying with the $(1/n)^2$-rate, cf. with the slopes of the magenta dashed lines in the same panels. When dealing with larger PCSEL devices requiring finer discretizations and, thus, substantial memory resources and processing time, it could be helpful to explore higher-order schemes [1]. A reasonable fourth-order scheme can be realized by replacing pretty simple operators σ_k^h and $\sigma_k^{\dagger h}$ in Equation (5.3) with more elaborated ones, acting differently for inner ($1 < k < n$) and boundary ($k = 1, n$) cells of the discretized domain:

$$\sigma_k^h V^h = \begin{cases} \frac{35V^h_{k-1}+140V^h_k-70V^h_{k+1}+28V^h_{k+2}-5V^h_{k+3}}{128} & \text{for } k=1,\\ \frac{9(V^h_k+V^h_{k-1})-(V^h_{k+1}+V^h_{k-2})}{8} & \text{for } 1<k<n,\\ \frac{35V^h_k+140V^h_{k-1}-70V^h_{k-2}+28V^h_{k-3}-5V^h_{k-4}}{128} & \text{for } k=n, \end{cases}$$

$$\sigma_k^{\dagger h} V^h = \begin{cases} \frac{-22V^h_{k-1}+17V^h_k+9V^h_{k+1}-5V^h_{k+2}+V^h_{k+3}}{24h} & \text{for } k=1,\\ \frac{27(V^h_k-V^h_{k-1})-(V^h_{k+1}-V^h_{k-2})}{24h} & \text{for } 1<k<n,\\ \frac{22V^h_k-17V^h_{k-1}-9V^h_{k-2}+5V^h_{k-3}-V^h_{k-4}}{24h} & \text{for } k=n. \end{cases}$$

These formulas are at least twice longer than those of (5.3), such that the corresponding matrices $\boldsymbol{H}_h$ and $\boldsymbol{D}_h$ in Equation (5.5) have more non-vanishing elements now. Shorter expressions within the inner cells can be explained by

the symmetry of the applied stencil w.r.t. the center of the cell where the approximation of the continuous functions and their derivatives is performed. In contrast, this symmetry is lost at the border cells, and the fourth-order approximations here use five mesh points. Loss of the symmetry also violates the conservation law (5.4). Similarly, one can also construct even higher $2s$-order schemes (5.1), which are defined by further modifications of operators σ_k^h and $\sigma_k^{\dagger h}$ which exploit $2s+1$ values of the grid function at $s-1$ outer cell layers, and $2s$ values of the same grid function within the remaining inner cells.

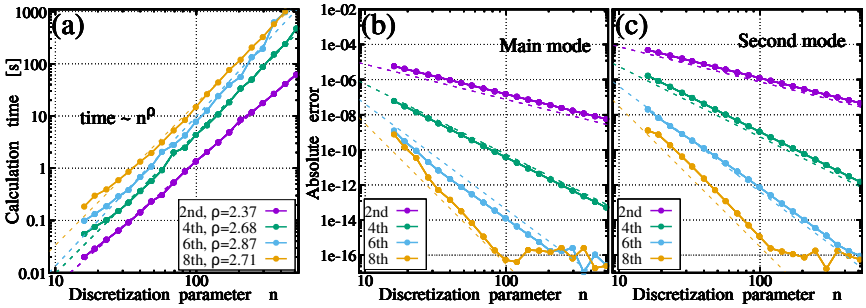

Figure 8. Comparison of schemes with different approximation orders used to calculate the five lowest threshold modes. Calculation time (a) and precision of calculated main (b) and the second (c) modes as functions of discretization parameter n. Dashed lines in (a): approximation of time by n^ρ; in (b) and (c): functions $10^{-4}e^s/n^s$ and $10^{-3}e^s/n^s$ with $s = 2, 4, 6, 8$, respectively.

The performance of different schemes is represented in Figure 8. Unlike our prior study shown in Figure 7, where all eigenvalues Λ_h of the discrete problem (5.1) were calculated, now we looked only for five major modes but could exploit fine numerical meshes generated using $n \le 512$ instead. Figure 8(a) shows the calculation time required to find these main modes using different approximations and discretization parameters n. In all cases, the simulation time grows with an increase of n as n^ρ, with ρ being between 2.3 and 2.9. We note a large gap between the times required by 2nd-order and 4th-order schemes compared to those of higher-order schemes. We attribute this difference to the trivial two-diagonal form of the matrix $\boldsymbol{D}_h$ in the 2nd order scheme (red dots in Figure 6), which is supplemented by additional diagonals and spoiled by the border-cell-induced asymmetries in the higher-order schemes.

Panels (b) and (c) of Figure 8 show a decay of the absolute errors $|\Lambda_h - \Lambda|$ of two major eigenvalues with the up-sweep of n. "Exact" eigenvalues Λ here were computed using the 8th-order scheme, $n = 1000$, and spectral shifts, enabling more accurate calculation of the eigenvalues close to their approximate positions Λ_h estimated in the preliminary calculation step on the less fine grid. The calculations show the expected convergence rate nicely, cf. with the dashed lines of the same color, indicating the expected error decay slopes for the schemes of corresponding order. This rate for higher order schemes is degraded once the error reaches 10^{-16}, the level at which approximations of Λ_h in the iterative procedure used by the spectral solver become indistinguishable.

From a practical perspective, these diagrams clearly demonstrate the advantages of higher-order schemes, even though they require up to ten times more calculation time for the same n. For example, the precision of 10^{-8} for the main mode, see panel (b), is achieved using $n \approx 390$ and 25 in the 2nd and 4th-order schemes, whereas the calculation time for these cases, see panel (a), is about 33 and 0.12 seconds, respectively. We have demonstrated, that for moderate-size PCSELs with $L < 1\,\mathrm{mm}$, as considered in our example, a good precision in calculating a few main modes can be achieved by exploring second- and higher-order schemes on relatively coarse meshes. For large-area PCSELs with L in the mm-cm range, we can use relatively coarse meshes for obtaining the aproximate mode landscape, as presented in Figure 7(b), and, when needed, to refine the precision of a few selected modes using fine (large n) meshes and/or the higher order schemes.

6 Conclusions

In this work, we addressed the practical problems arising during the construction of the mathematical model for novel PCSEL devices, which, up to our knowledge, were not discussed yet in the (mainly engineering) papers on PCSELs. Namely, we gave a detailed description of the algorithms to construct the field cross-coupling matrices $\boldsymbol{C}$, indicated possible numerical problems related to the limitations of computer arithmetics when dealing with the huge and tiny values of the exponential functions, and presented methods for avoiding these limitations. Our algorithms for constructing $\boldsymbol{C}$ rely on analytic formulas. They are precise and much more efficient than fully numerical approaches and allow us to account for a much larger number of submatrices $\boldsymbol{C}_{2D}^{(r,s)}$ in the infinite series used for the definition of $\boldsymbol{C}_{2D}$ and $\boldsymbol{C}$. Next, we constructed the 2nd-order finite difference scheme for the spectral problem. After deriving a discrete analog of the integral conservation law, we demonstrated the performance of this scheme in solving the spectral problem for a selected PCSEL device. We have shown that even the schemes with relatively coarse numerical meshes can provide decent approximations of several main eigenvalues of the original problem. Finally, we have also constructed the higher order schemes, which can be preferable if a better precision of calculated spectra is required, many similar spectral calculations should be performed in a limited time, or spectral calculations of PCSELs with a huge emission area (large L) are needed.

Acknowledgements

This work was performed in the frame of the project "PCSELence" (K487/2022) funded by the German Leibniz Association. We are indebted to P. Crump and B. King (FBH) for initiating this study.

References

[1] N.S. Bakhvalov, G.M. Kobel'kov and N.P. Zhidkov. *Chislennye metody.* Fizmatlit, Moscow, 2000 (in Russian).

[2] M.J. Bergmann and H.C. Casey. Optical-field calculations for lossy multiple-layer $Al_xGa_{1-x}N/In_xGa_{1-x}N$ laser diodes. *Journal of Applied Physics*, **84**(3):1196–1203, 1998. https://doi.org/10.1063/1.368185.

[3] J. Bezanson, A. Edelman, S. Karpinski and V.B. Shah. Julia: A fresh approach to numerical computing. *SIAM review*, **59**(1):65–98, 2017. https://doi.org/10.1137/141000671.

[4] J. Chilwell and I. Hodgkinson. Thin-films field-transfer matrix theory of planar multilayer waveguides and reflection from prism-loaded waveguides. *Journal of the Optical Society of America A*, **1**(7):742–753, 1984. https://doi.org/10.1364/JOSAA.1.000742.

[5] M. Imada, S. Noda, A. Chutinan, T. Tokuda, M. Murata and G. Sasaki. Coherent two-dimensional lasing action in surface-emitting laser with triangular-lattice photonic crystal structure. *Applied Physics Letters*, **75**(3):316–318, 1999. https://doi.org/10.1063/1.124361.

[6] T. Inoue, R. Morita, M. Yoshida, M. De Zoysa, Y. Tanaka and S. Noda. Comprehensive analysis of photonic-crystal surface-emitting lasers via time-dependent three-dimensional coupled-wave theory. *Physical Review B*, **99**(3):035308, 2019. https://doi.org/10.1103/PhysRevB.99.035308.

[7] Y. Liang, C. Peng, K. Sakai, S. Iwahashi and S. Noda. Three-dimensional coupled-wave analysis for square-lattice photonic crystal surface emitting lasers with transverse-electric polarization: finite-size effects. *Optics Express*, **20**(14):15945–15961, 2012. https://doi.org/10.1364/OE.20.015945.

[8] C. Peng, Y. Liang, K. Sakai, S. Iwahashi and S. Noda. Coupled-wave analysis for photonic-crystal surface-emitting lasers on air holes with arbitrary sidewalls. *Optics Express*, **19**(24):24672–24686, 2011. https://doi.org/10.1364/OE.19.024672.

[9] M. Radziunas and R. Čiegis. Effective numerical algorithm for simulations of beam stabilization in broad area semiconductor lasers and amplifiers. *Mathematical Modelling and Analysis*, **19**(5):627–646, 2014. https://doi.org/10.3846/13926292.2014.979453.

[10] M. Radziunas and H.-J. Wünsche. Multisection lasers: Longitudinal modes and their dynamics. In J. Piprek(Ed.), *Optoelectronic Devices - Advanced Simulation and Analysis*, chapter 5, pp. 121–150. Springer, New York, 2005. https://doi.org/10.1007/0-387-27256-9_5.

[11] M. Yoshida, S. Katsuno, T. Inoue, J. Gelleta, K. Izumi, M. De Zoysa, K. Ishizaki and S. Noda. High-brightness scalable continuous-wave single-mode photonic-crystal laser. *Nature*, **618**(7966):727—732, 2023. https://doi.org/10.1038/s41586-023-06059-8.

[12] A. Zeghuzi, M. Radziunas, H.-J. Wünsche, J.-P. Koester, H. Wenzel, U. Bandelow and A. Knigge. Traveling wave analysis of non-thermal far-field blooming in high-power broad-area lasers. *IEEE Journal of Quantum Electronics*, **55**(2):2000207, 2019. https://doi.org/10.1109/JQE.2019.2893352.

[13] A. Zeghuzi, H.-J. Wünsche, H. Wenzel, M. Radziunas, J. Fuhrmann, A. Klehr, U. Bandelow and A. Knigge. Time-dependent simulation of thermal lensing in high-power broad-area semiconductor lasers. *IEEE Journal of Selected Topics in Quantum Electronics*, **25**(6):1502310, 2019. https://doi.org/10.1109/JSTQE.2019.2925926.